

AI optimization and mathematical simulation validated by nondestructive testing for resonance frequency in advanced composite structures for bridge applications

Wenjie Yang, Gongxing Yan, Khalid A. Alnowibet & Mohammed El-Meligy

To cite this article: Wenjie Yang, Gongxing Yan, Khalid A. Alnowibet & Mohammed El-Meligy (15 Oct 2024): AI optimization and mathematical simulation validated by nondestructive testing for resonance frequency in advanced composite structures for bridge applications, Mechanics of Advanced Materials and Structures, DOI: [10.1080/15376494.2024.2404994](https://doi.org/10.1080/15376494.2024.2404994)

To link to this article: <https://doi.org/10.1080/15376494.2024.2404994>



Published online: 15 Oct 2024.



Submit your article to this journal [↗](#)



Article views: 6



View related articles [↗](#)



View Crossmark data [↗](#)

AI optimization and mathematical simulation validated by nondestructive testing for resonance frequency in advanced composite structures for bridge applications

Wenjie Yang^{a,b}, Gongxing Yan^{c,d}, Khalid A. Alnowibet^e, and Mohammed El-Meligy^{f,g}

^aSchool of Materials Science and Engineering, Wuhan Institute of Technology, Wuhan, China; ^bSichuan Jinghengxin Construction Engineering Testing Co., Ltd, Luzhou, China; ^cSchool of Intelligent Construction, Luzhou Vocational and Technical College, Luzhou, China; ^dLuzhou Key Laboratory of Intelligent Construction and Low-carbon Technology, Luzhou, China; ^eStatistics and Operations Research Department, College of Science, King Saud University, Riyadh, Kingdom of Saudi Arabia; ^fJadara University Research Center, Jadara University, Irbid, Jordan; ^gApplied Science Research Center, Applied Science Private University, Amman, Jordan

ABSTRACT

This paper presents a novel approach integrating artificial intelligence (AI) optimization and mathematical simulation to predict the resonance frequency of nanoclay-reinforced concrete cylindrical shell structures intended for bridge applications. These composite structures, known for their enhanced mechanical properties, require precise evaluation of their vibrational behavior to ensure structural stability and longevity. Traditional methods for predicting resonance frequencies are often time-consuming and prone to inaccuracies, especially in complex materials like nanoclay composites. To address this, an AI-based optimization algorithm was developed, incorporating Particle Swarm Optimization (PSO) and a mathematical modeling to simulate resonance characteristics under varying material and geometric parameters. The mathematical modeling is validated using nondestructive testing (NDT) techniques, such as modal analysis, which provided real-world resonance data without damaging the structure. The nondestructive testing results is compared against the mathematical model to ensure accuracy and reliability. The integration of nanoclay into the concrete matrix significantly altered the vibrational properties, enhancing the stiffness and reducing damping losses, which is crucial for bridge applications where dynamic loads are prevalent. The optimized model not only predicted resonance frequencies with high accuracy but also demonstrated its potential for large-scale bridge infrastructure. This methodology offers a streamlined and robust tool for engineers, reducing the need for physical prototyping and providing enhanced design capabilities. Future research will focus on expanding the model to incorporate additional material behaviors and load conditions, furthering its application in civil engineering.

ARTICLE HISTORY

Received 9 July 2024
Accepted 11 September 2024

KEYWORDS

Optimization; simulation; resonance frequency; nanoclay-reinforcement; concrete cylindrical shell structure

1. Introduction

Advanced composites are crucial for engineers due to their remarkable properties. They provide an enhanced strength-to-weight ratio, allowing for lighter yet stronger structures [1, 2]. This improvement translates into increased efficiency and performance in various applications. Composites also exhibit superior durability, resisting corrosion, wear, and environmental degradation, which leads to reduced maintenance and longer service life. The design flexibility offered by composites is unmatched; engineers can customize fiber orientations and matrix materials to meet specific requirements [3, 4]. Thermal resistance is another critical advantage, as these materials withstand extreme temperatures, making them ideal for aerospace and automotive industries [5, 6]. Advanced composites also excel in vibration damping, contributing to smoother and more comfortable mechanical systems [7]. Their fatigue resistance ensures that components can endure repeated stress without failure, extending their

operational lifespan [8]. Additionally, the impact resistance of composites enhances safety by protecting structures from sudden forces [9]. Composites are also highly resistant to chemical attacks, which is vital for applications in harsh environments [10, 11]. Their low thermal expansion minimizes dimensional changes with temperature fluctuations, maintaining structural integrity [12]. The versatility in manufacturing techniques, such as molding and layering, allows for complex shapes and designs that traditional materials cannot achieve [13]. Engineers benefit from the reduced weight of composites, which can lead to fuel savings and lower emissions in transportation sectors [14]. The customization of properties such as stiffness and strength allows for precise control over material performance [15]. Advanced composites also support innovative engineering solutions, enabling the development of new products and technologies [16]. Their use contributes to sustainable engineering practices by reducing material waste and improving energy efficiency

[17]. The integration of advanced composites into engineering projects represents a significant advancement in materials science, driving progress across multiple industries [18, 19]. As research and technology continue to evolve, the potential applications and benefits of advanced composites will expand, offering engineers even more opportunities for innovation and improvement [20].

The seismic performance of structures is vital for engineers due to several crucial reasons [21, 22]. First, it directly impacts safety by ensuring that buildings and infrastructure can withstand earthquakes, protecting lives and reducing the risk of injury or fatalities [23, 24]. Second, maintaining structural integrity during seismic events prevents catastrophic failures, preserving the stability of critical infrastructure and reducing damage [25, 26]. Third, engineers must design structures to remain functional after an earthquake, facilitating quick recovery and minimizing disruption to communities and essential services [14, 27]. Fourth, effective seismic performance reduces the economic impact of earthquakes by lowering repair and reconstruction costs [15, 28]. Fifth, it enhances the resilience of infrastructure, enabling it to perform reliably under seismic loads [29, 30]. Sixth, considering seismic performance in design helps in meeting building codes and regulatory requirements, ensuring compliance and avoiding legal issues [31, 32]. Seventh, it supports the longevity of structures, extending their service life and protecting investments [33, 34]. Eighth, seismic performance contributes to the overall durability of buildings, reducing maintenance needs and associated costs [35, 36]. Ninth, it fosters public confidence in the safety and reliability of infrastructure, which is crucial for community trust and well-being [37, 38]. Tenth, engineers can use advanced materials and construction techniques to improve seismic performance, leading to innovative design solutions [39, 40]. Eleventh, effective seismic design minimizes the risk of secondary hazards, such as fires or gas leaks, that can occur after structural damage [41, 42]. Twelfth, it allows for the incorporation of retrofitting strategies in existing structures, enhancing their earthquake resistance [43, 44]. Thirteenth, good seismic performance supports the efficient use of resources by optimizing material usage and construction methods [45, 46]. Fourteenth, it aids in the development of resilient urban planning, integrating seismic considerations into the broader context of city design [47, 48]. Fifteenth, engineers can use simulation and modeling tools to predict and enhance seismic behavior, leading to more effective designs [49, 50]. Sixteenth, proper seismic design contributes to the sustainability of infrastructure by reducing the need for frequent repairs and replacements [51]. Seventeenth, it helps protect cultural heritage by ensuring that historic buildings and monuments can withstand earthquakes [52]. Eighteenth, understanding seismic performance supports the development of safety guidelines and emergency preparedness plans [53]. Nineteenth, it enhances the ability to design structures that can be rapidly evacuated or repurposed after an earthquake [54]. Twentieth, ongoing research and advancements in seismic engineering continue to improve

the effectiveness of design practices, contributing to safer and more resilient communities [55].

In order to forecast the resonance frequency of concrete cylinder shell constructions reinforced with nanoclay that are meant for use as bridges, this research provides a unique method that combines mathematical modeling with artificial intelligence optimization. Because of their improved mechanical qualities, these composite constructions need to have their vibrational behavior precisely evaluated in order to guarantee structural lifetime and stability. Conventional techniques for estimating resonance frequencies are often laborious and prone to error, particularly when dealing with intricate materials like nanoclay composites. An AI-based optimization approach was created to solve this, combining mathematical modeling to replicate resonance characteristics under altering material and geometric factors with Particle Swarm Optimization. Nondestructive testing methods, such as modal analysis, which produced real-world resonance data without endangering the structure, are used to verify the mathematical models. The correctness and reliability of the nondestructive testing findings are verified by comparing them with the mathematical model. For bridge applications where dynamic loads are common, the incorporation of nanoclay into the concrete matrix dramatically changed the vibrational characteristics by increasing stiffness and decreasing damping losses. The refined model showed promise for extensive bridge infrastructure in addition to its high accuracy resonance frequency prediction. This technique reduces the need for physical prototypes and gives engineers a sturdy and efficient tool with improved design capabilities. To further enhance the model's usefulness in civil engineering, future research will concentrate on adding other material behaviors and load circumstances.

2. Mathematical modeling

2.1. Material properties of the nanoclay composites reinforced concrete shell structure

These days, one of the materials most often used in industry is a composite made of polymers. These materials are gaining a lot of interest in the aerospace, military, and aviation sectors because of their strong mechanical qualities and notable weight reduction in structural design. Special qualities including high strength-to-weight ratio, fatigue resistance, and wear resistance [56] set composite materials apart from conventional metallic alloys. Additionally, a cylindrical shell, represented by the letter L , is taken into consideration in this research. As seen in [Figure 1](#), the average radius and shell thickness are R and h , respectively.

2.2. Elasticity modulus using the Halpin-Tsai model

The elastic modulus of composite materials, such as nanoclay-reinforced composites, is often predicted using the Halpin-Tsai model. The reinforcement's distribution, form, and orientation within the matrix are all taken into consideration by this model. The effective Young's modulus, E_c , of

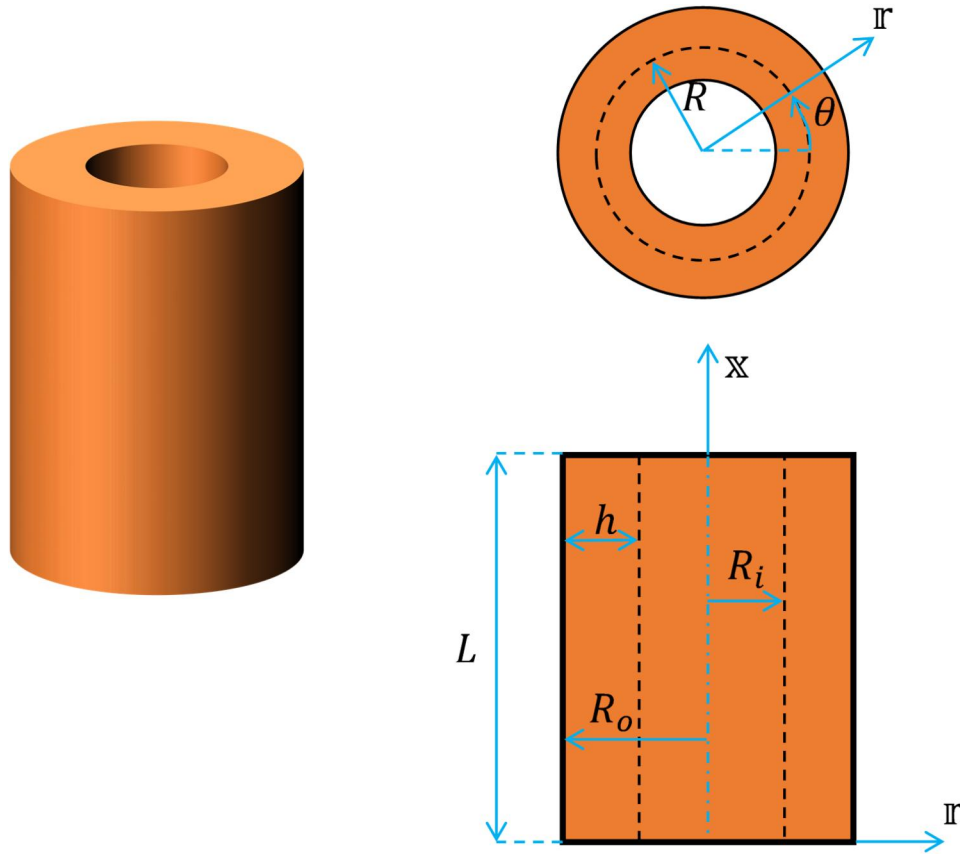


Figure 1. Geometry and coordinate system of a reinforced concrete shell construction using nanoclay composites.

a composite reinforced by nanoclay may be approximated as follows:

$$E_c = E_m \times ((1 + 2\eta W_{NC}) / (1 - \eta W_{NC})), \quad (1)$$

where:

E_c = Effective Young's modulus of the composite.

E_m = Young's modulus of the matrix material.

W_{NC} = Volume fraction of the nanoclay.

η = Reinforcement efficiency parameter, defined as:

$$\eta = ((E_f/E_m) - 1) / ((E_f/E_m) - 2\zeta), \quad (2)$$

where:

E_f = Young's modulus of the nanoclay.

ζ = A parameter depending on the shape and orientation of the nanoclay particles. For platelets like nanoclay, ζ is often taken.

2.3. Other material properties

The Poisson's ratio of the composite can be estimated as:

$$\vartheta_c = \vartheta_m \times (1 - W_{NC}) + \vartheta_f \times W_{NC}, \quad (3)$$

where:

ϑ_c = Poisson's ratio of the composite.

ϑ_m = Poisson's ratio of the matrix.

ϑ_f = Poisson's ratio of the nanoclay.

The density of the composite is given by:

$$\rho_c = \rho_m \times (1 - W_{NC}) + \rho_f \times W_{NC}, \quad (4)$$

where:

ρ_c = Density of the composite.

ρ_m = Density of the matrix.

ρ_f = Density of the nanoclay.

2.4. Distribution pattern of nanoclays along with thickness direction

The mechanical, thermal, and barrier characteristics of a composite structure may be greatly impacted by the distribution of nanoclay. The volume fraction, or the ratio of the nanoclay volume to the overall volume of the composite material, is often used to assess the effect of nanoclay dispersion. The function of nanoclay dispersion changes with volume fraction in the following ways in various directions (such as along the thickness and in-plane):

$$\text{Pattern O : } V_{NC}(z) = 2 \left(1 - \frac{|z|}{h} \right) V_{NC}^*, \quad (5a)$$

$$\text{Pattern UD : } V_{NC}(z) = V_{NC}^*, \quad (5b)$$

$$\text{Pattern X : } V_{NC}(z) = 4 \frac{|z|}{h} V_{NC}^*, \quad (5c)$$

where the total volume percentage of nanoclays is denoted by V_{NC}^* . It remains steady and unaffected by the

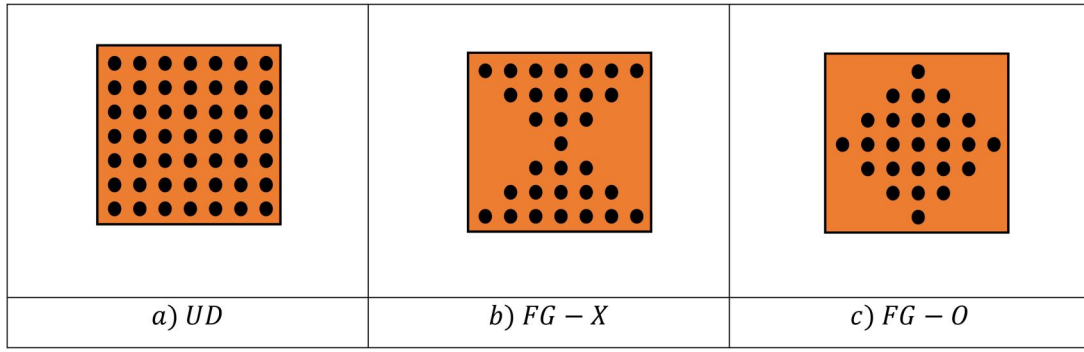


Figure 2. Various distribution patterns of nanoclays.

Table 1. Mechanical properties of the two components of the matrix and the reinforced [57].

Property name	Matrix	Nanoclay
Modulus of elasticity (E) [GPa]	25	178
Density (ρ) [kg/m^3]	2300	2580
Poisson's ratio (ν)	0.2	0.25

distributions of nanoclays. It may be expressed like this:

$$V_{NC}^* = \frac{W_{NC}}{W_{NC} + \rho_c/\rho_m - W_{NC}\rho_c/\rho_m}. \quad (6)$$

Various distribution patterns of nanoclays are shown in Figure 2.

The properties of the materials used are presented in Table 1.

2.5. Kinematic relations and energy expressions

The linear strain-displacement connections may be explained using the 3-D shell theory of elasticity as,

$$\varepsilon_x = \frac{\partial u}{\partial x}, \varepsilon_\theta = \frac{\partial v}{r\partial\theta} + \frac{w}{r}, \varepsilon_r = \frac{\partial w}{\partial r}, \quad (7a)$$

$$\gamma_{\theta r} = \frac{\partial w}{r\partial\theta} + \frac{\partial v}{\partial r} - \frac{v}{r}, \gamma_{xr} = \frac{\partial u}{\partial r} + \frac{\partial w}{\partial x}, \gamma_{x\theta} = \frac{\partial u}{r\partial\theta} + \frac{\partial v}{\partial x}. \quad (7b)$$

where ε_x , ε_θ and ε_r represent the normal stresses; $\gamma_{\theta r}$, γ_{xr} and $\gamma_{x\theta}$ indicate the shear strains; and u , v and w indicate the displacement components in the x (axial), θ (circumferential), and r (radial) directions. Given Hooke's law, the overall stress-strain relationships may be expressed as

$$\begin{Bmatrix} \sigma_x \\ \sigma_\theta \\ \sigma_r \\ \mathcal{T}_{\theta r} \\ \mathcal{T}_{xr} \\ \mathcal{T}_{x\theta} \end{Bmatrix} = \begin{bmatrix} Q_{11} & Q_{12} & Q_{13} & 0 & 0 & 0 \\ Q_{12} & Q_{22} & Q_{23} & 0 & 0 & 0 \\ Q_{13} & Q_{23} & Q_{33} & 0 & 0 & 0 \\ 0 & 0 & 0 & Q_{44} & 0 & 0 \\ 0 & 0 & 0 & 0 & Q_{55} & 0 \\ 0 & 0 & 0 & 0 & 0 & Q_{66} \end{bmatrix} \begin{Bmatrix} \varepsilon_x \\ \varepsilon_\theta \\ \varepsilon_r \\ \gamma_{\theta r} \\ \gamma_{xr} \\ \gamma_{x\theta} \end{Bmatrix}. \quad (8)$$

where σ_x , σ_θ and σ_r signify normal stresses; $\mathcal{T}_{\theta r}$, \mathcal{T}_{xr} and $\mathcal{T}_{x\theta}$ express the shear stresses; Q_{ij} ($i, j = 1 - 6$) represent the elastic constants, which can be represented as

$$Q_{11} = Q_{22} = Q_{33} = \frac{E_c(1 - \nu_c)}{(1 + \nu_c)(1 - 2\nu_c)}, \quad (9a)$$

$$Q_{12} = Q_{13} = Q_{23} = \frac{\nu_c E_c}{(1 + \nu_c)(1 - 2\nu_c)},$$

$$Q_{44} = Q_{55} = Q_{66} = \frac{E_c}{2(1 + \nu_c)}. \quad (9b)$$

Following the kinematic relations, the strain energy U_V of the composite structure is manifested as follows:

$$\begin{aligned} U_V &= \frac{1}{2} \int_V (\sigma_x \varepsilon_x + \sigma_r \varepsilon_r + \sigma_\theta \varepsilon_\theta + \mathcal{T}_{\theta r} \gamma_{\theta r} + \mathcal{T}_{xr} \gamma_{xr} + \mathcal{T}_{x\theta} \gamma_{x\theta}) dV \\ &= \frac{1}{2} \int_V \left\{ Q_{11} \left(\frac{\partial u}{\partial x} \right)^2 + 2Q_{12} \frac{\partial u}{\partial x} \left(\frac{\partial v}{r\partial\theta} + \frac{w}{r} \right) + 2Q_{13} \frac{\partial u}{\partial x} \frac{\partial w}{\partial r} + Q_{22} \left(\frac{\partial v}{r\partial\theta} + \frac{w}{r} \right)^2 + 2Q_{23} \left(\frac{\partial v}{r\partial\theta} + \frac{w}{r} \right) \frac{\partial w}{\partial r} + Q_{33} \left(\frac{\partial w}{\partial r} \right)^2 \right. \\ &\quad \left. + Q_{44} \left(\frac{\partial w}{r\partial\theta} + \frac{\partial v}{\partial r} - \frac{v}{r} \right)^2 + Q_{55} \left(\frac{\partial u}{\partial r} + \frac{\partial w}{\partial x} \right)^2 + Q_{66} \left(\frac{\partial u}{r\partial\theta} + \frac{\partial v}{\partial x} \right)^2 \right\} dV. \end{aligned} \quad (10)$$

To replicate the boundary conditions, a set of continuously distributed boundary springs is used in this study [58]. Three sets of linear springs with stiffnesses κ_{u0} , κ_{v0} and κ_{w0} (or κ_{uL} , κ_{vL} and κ_{wL}) are inserted at edge $x = 0$ (or edge $x = L$). One may generate varied boundary conditions by varying the values of each stiffness. The boundary springs' conserved potential energy \mathbb{U}_S is,

$$\mathbb{U}_S = \frac{1}{2} \int_0^h \int_0^{2\pi} \left\{ [\kappa_{u0} u^2 + \kappa_{v0} v^2 + \kappa_{w0} w^2] \Big|_{x=0} + [\kappa_{uL} u^2 + \kappa_{vL} v^2 + \kappa_{wL} w^2] \Big|_{x=L} \right\} r d\theta dr. \quad (11)$$

As previously stated, mechanical stress and Winkler-Pasternak elastic foundations are taken into account. The following represents the potential energy associated with the three elastic foundations \mathbb{U}_F :

$$\mathbb{U}_{F,WP} = \frac{1}{2} \int_0^L \int_0^{2\pi} \left\{ K_W w^2 + K_P \left[\left(\frac{\partial w}{\partial x} \right)^2 + \left(\frac{\partial w}{r \partial \theta} \right)^2 \right] \right\} \Big|_{r=R_0} R_0 d\theta dx, \quad (12a)$$

$$\mathbb{U}_{F,P} = \frac{1}{2} \int_0^L \int_0^{2\pi} \left\{ P^* \left[\left(\frac{\partial w}{\partial x} \right)^2 + \left(\frac{\partial w}{r \partial \theta} \right)^2 \right] \right\} \Big|_{r=R_0} R_0 d\theta dx. \quad (12b)$$

where $\mathbb{U}_{F,WP}$ represent the potential energy in correspondence with Winkler-Pasternak foundations, and $\mathbb{U}_{F,P}$ indicate potential energy with mechanical load respectively.

In addition, the kinetic energy \mathbb{T} can be depicted as,

$$\mathbb{T} = \int_0^h \int_0^{2\pi} \int_0^L \frac{\rho_c}{2} \left\{ \left(\frac{\partial u}{\partial t} \right)^2 + \left(\frac{\partial v}{\partial t} \right)^2 + \left(\frac{\partial w}{\partial t} \right)^2 \right\} r dx d\theta dr. \quad (13)$$

2.6. Admissible displacement functions and unified solution

In this part, six distinct categories of acceptable functions are selected for comparison. These recursive formulas of order i and variable \mathfrak{A} may be represented as $\mathfrak{H}_i(\mathfrak{A})$. It should be noted that the intervals of \mathfrak{A} vary for various polynomials, hence the following equations can be provided:

1. Chebyshev polynomials of first kind (Chebyshev I) [59]

$$\begin{aligned} \mathfrak{H}_0(\mathfrak{B}) &= 1, \mathfrak{H}_1(\mathfrak{B}) = \mathfrak{B}, \mathfrak{H}_i(\mathfrak{B}) \\ &= 2\mathfrak{B}\mathfrak{H}_{i-1}(\mathfrak{B}) - \mathfrak{H}_{i-2}(\mathfrak{B}), i \geq 2, \mathfrak{B} \in [-1, 1]. \end{aligned} \quad (14)$$

2. Chebyshev polynomials of second kind (Chebyshev II) [59]:

$$\begin{aligned} \mathfrak{H}_0(\mathfrak{B}) &= 1, \mathfrak{H}_1(\mathfrak{B}) = 2\mathfrak{B}, \mathfrak{H}_i(\mathfrak{B}) \\ &= 2\mathfrak{B}\mathfrak{H}_{i-1}(\mathfrak{B}) - \mathfrak{H}_{i-2}(\mathfrak{B}), i \geq 2, \mathfrak{B} \in [-1, 1]. \end{aligned} \quad (15)$$

3. Legendre polynomials [59]:

$$\begin{aligned} \mathfrak{H}_0(\mathfrak{B}) &= 1, \mathfrak{H}_1(\mathfrak{B}) = 2\mathfrak{B}, \mathfrak{H}_i(\mathfrak{B}) \\ &= \frac{2i-1}{i} \mathfrak{B}\mathfrak{H}_{i-1}(\mathfrak{B}) - \frac{(i-1)}{i} \mathfrak{H}_{i-2}(\mathfrak{B}), i \geq 2, \\ &\mathfrak{B} \in [-1, 1] \end{aligned} \quad (16)$$

4. Orthogonal polynomials [60]:

$$\mathfrak{H}_0(\mathfrak{B}) = 1, \mathfrak{H}_i(\mathfrak{B}) = \frac{\mathfrak{C}_i(\mathfrak{B})}{\sqrt{\int_0^1 [\mathfrak{C}_i(\mathfrak{B})]^2 d\mathfrak{B}}}, i \geq 1. \quad (17)$$

where $\mathfrak{C}_i(\mathfrak{B})$ are a set of polynomials which are orthogonal. The corresponding recursive formulas can be constructed as below

$$\begin{cases} \mathfrak{C}_1(B) = 1, \mathfrak{C}_2(B) = (B - \mathfrak{B}_1)\mathfrak{C}_1(B) \\ \mathfrak{C}_{i+1}(B) = (B - \mathfrak{B}_i)\mathfrak{C}_i(B) - \mathfrak{C}_i\mathfrak{C}_{i-1}(B), i \geq 2 \end{cases}, \mathfrak{B} \in [0, 1]. \quad (18)$$

where

$$\mathfrak{B}_i = \frac{\int_0^1 \mathfrak{B} [\mathfrak{C}_i(\mathfrak{B})]^2 d\mathfrak{B}}{\int_0^1 [\mathfrak{C}_i(\mathfrak{B})]^2 d\mathfrak{B}}, \mathfrak{C}_i = \frac{\int_0^1 \mathfrak{B} \mathfrak{C}_i(\mathfrak{B}) \mathfrak{C}_{i-1}(\mathfrak{B}) d\mathfrak{B}}{\int_0^1 [\mathfrak{C}_{i-1}(\mathfrak{B})]^2 d\mathfrak{B}}. \quad (19)$$

5. Modified Fourier series of first kind (Modified Fourier I) [61]:

$$\mathfrak{H}_i(\mathfrak{B}) = \begin{cases} \sin \frac{(i-3)\pi}{a} \mathfrak{B}, 1 \leq i \leq 2 \\ \cos \frac{(i-3)\pi}{a} \mathfrak{B}, i > 2 \end{cases}. \quad (20)$$

In x direction, $a = L$, $\mathfrak{A} \in [0, L]$; in r direction, $a = h$, $\mathfrak{A} \in [0, h]$. It is worth noting that when $i = 1$ and 2 , two supplementary terms with sinusoidal form are exerted to assure the second-derivatives of admissible functions.

6. Modified Fourier series of second kind (Modified Fourier II) [62]:

$$\begin{aligned} \mathfrak{H}_1(\mathfrak{B}) &= \mathfrak{B} \left(\frac{\mathfrak{B}}{a} - 1 \right), \mathfrak{H}_2(\mathfrak{B}) = \frac{\mathfrak{B}^2}{a} \left(\frac{\mathfrak{B}}{a} - 1 \right), \\ \mathfrak{H}_i(\mathfrak{B}) &= \cos \frac{(i-3)\pi}{a} \mathfrak{B}, i \geq 3 \end{aligned} \quad (21)$$

In x direction, $a = L$, $\mathfrak{A} \in [0, L]$; in r direction, $a = h$, $\mathfrak{A} \in [0, h]$. Again, two additional terms \mathfrak{H}_1 and \mathfrak{H}_2 are added to deal with any possible discontinuities.

The displacement fields of the composite structures can be presented in a general form as:

$$u = \sum_{\bar{m}=0}^M \sum_{\bar{n}=0}^N \mathfrak{H}_{\bar{m}}(\mathfrak{B}_x) \mathfrak{H}_{\bar{n}}(\mathfrak{B}_r) [\mathbb{U}_{\bar{m}\bar{n}}^c \cos(n\theta) + \mathbb{U}_{\bar{m}\bar{n}}^s \sin(n\theta)] e^{i\omega t}, \quad (22a)$$

$$\mathbf{v} = \sum_{\bar{m}=0}^M \sum_{\bar{n}=0}^N \mathfrak{H}_{\bar{m}}(\mathfrak{B}_x) \mathfrak{H}_{\bar{n}}(\mathfrak{B}_r) [\mathbb{V}_{\bar{m}\bar{n}}^c \cos(n\theta) + \mathbb{V}_{\bar{m}\bar{n}}^s \sin(n\theta)] e^{i\omega t}, \quad (22b)$$

$$\mathbf{w} = \sum_{\bar{m}=0}^M \sum_{\bar{n}=0}^N \mathfrak{H}_{\bar{m}}(\mathfrak{B}_x) \mathfrak{H}_{\bar{n}}(\mathfrak{B}_r) [\mathbb{W}_{\bar{m}\bar{n}}^c \cos(n\theta) + \mathbb{W}_{\bar{m}\bar{n}}^s \sin(n\theta)] e^{i\omega t}. \quad (22c)$$

where $\mathbb{U}_{\bar{m}\bar{n}}^c$, $\mathbb{U}_{\bar{m}\bar{n}}^s$, $\mathbb{V}_{\bar{m}\bar{n}}^c$, $\mathbb{V}_{\bar{m}\bar{n}}^s$, $\mathbb{W}_{\bar{m}\bar{n}}^c$ and $\mathbb{W}_{\bar{m}\bar{n}}^s$ are unknown expanded coefficients; M and N are the maximum values of \bar{m} and \bar{n} , respectively; n indicates the circumferential wave number; ω is the angular frequency and t is the time; $\mathfrak{H}_{\bar{m}}(\mathfrak{B}_x)$ and $\mathfrak{H}_{\bar{n}}(\mathfrak{B}_r)$ are the polynomials of degree \bar{m} in the length direction and of degree \bar{n} in the radial direction, respectively. The expressions of them are

$$\mathfrak{H}_{\bar{m}} = [\mathfrak{H}_0(\mathfrak{B}_x), \mathfrak{H}_1(\mathfrak{B}_x), \dots, \mathfrak{H}_{\bar{m}}(\mathfrak{B}_x), \dots, \mathfrak{H}_M(\mathfrak{B}_x)], \quad (23a)$$

$$\mathfrak{H}_{\bar{n}} = [\mathfrak{H}_0(\mathfrak{B}_r), \mathfrak{H}_1(\mathfrak{B}_r), \dots, \mathfrak{H}_{\bar{n}}(\mathfrak{B}_r), \dots, \mathfrak{H}_N(\mathfrak{B}_r)]. \quad (23b)$$

The \mathfrak{B}_x and \mathfrak{B}_r are dimensionless coordinate in the x and r directions, respectively. They are obtained from linear transformations of x and r , since different polynomials are defined in diverse intervals. For Chebyshev I, II and Legendre polynomials,

$$\mathfrak{B}_x = 2x/L - 1, \mathfrak{B}_r = 2r/h - 1, \quad (24)$$

For Orthogonal polynomials and Fourier-Bessel series,

$$\mathfrak{B}_x = \frac{2x}{L}, \mathfrak{B}_r = \frac{2r}{h}, \quad (25)$$

For Modified Fourier I and II,

$$\mathfrak{B}_x = x, \mathfrak{B}_r = r, \quad (26)$$

Then, the unified forms of admissible displacement functions can be represented as,

$$\mathbf{u} = \mathbf{U} \cdot \mathfrak{g}_u, \mathbf{v} = \mathbf{V} \cdot \mathfrak{g}_v, \mathbf{w} = \mathbf{W} \cdot \mathfrak{g}_w, \quad (27)$$

$$\mathbf{U} = \left\{ \begin{array}{l} \mathfrak{H}_0(\mathfrak{B}_x) \mathfrak{H}_0(\mathfrak{B}_r) \cos(n\theta), \dots, \mathfrak{H}_{\bar{m}}(\mathfrak{B}_x) \mathfrak{H}_{\bar{n}}(\mathfrak{B}_r) \cos(n\theta), \dots, \mathfrak{H}_M(\mathfrak{B}_x) \mathfrak{H}_N(\mathfrak{B}_r) \cos(n\theta) \\ \mathfrak{H}_0(\mathfrak{B}_x) \mathfrak{H}_0(\mathfrak{B}_r) \sin(n\theta), \dots, \mathfrak{H}_{\bar{m}}(\mathfrak{B}_x) \mathfrak{H}_{\bar{n}}(\mathfrak{B}_r) \sin(n\theta), \dots, \mathfrak{H}_M(\mathfrak{B}_x) \mathfrak{H}_N(\mathfrak{B}_r) \sin(n\theta) \end{array} \right\}, \quad (28a)$$

where

$$\mathbf{V} = \mathbf{W} = \mathbf{U}, \quad (28b)$$

$$\mathfrak{g}_u = \{ \mathbb{U}_{00}^c, \dots, \mathbb{U}_{\bar{m}\bar{n}}^c, \dots, \mathbb{U}_{MN}^c, \mathbb{U}_{00}^s, \dots, \mathbb{U}_{\bar{m}\bar{n}}^s, \dots, \mathbb{U}_{MN}^s \} e^{i\omega t}, \quad (28c)$$

$$\mathfrak{g}_v = \{ \mathbb{V}_{00}^c, \dots, \mathbb{V}_{\bar{m}\bar{n}}^c, \dots, \mathbb{V}_{MN}^c, \mathbb{V}_{00}^s, \dots, \mathbb{V}_{\bar{m}\bar{n}}^s, \dots, \mathbb{V}_{MN}^s \} e^{i\omega t}, \quad (28d)$$

$$\mathfrak{g}_w = \{ \mathbb{W}_{00}^c, \dots, \mathbb{W}_{\bar{m}\bar{n}}^c, \dots, \mathbb{W}_{MN}^c, \mathbb{W}_{00}^s, \dots, \mathbb{W}_{\bar{m}\bar{n}}^s, \dots, \mathbb{W}_{MN}^s \} e^{i\omega t}. \quad (28e)$$

Currently, the Rayleigh-Ritz approach may be used to carry out the solution operation. The composite structure's Lagrangian energy function may be shown as,

$$\mathbb{L} = \mathbb{U}_V + \mathbb{U}_S + \mathbb{U}_F - \mathbb{T}. \quad (29)$$

Then the \mathbb{L} is minimized with respect to unknown expanded coefficient ϑ ($=\mathbb{U}_{\bar{m}\bar{n}}$, $\mathbb{V}_{\bar{m}\bar{n}}$ and $\mathbb{W}_{\bar{m}\bar{n}}$) as below:

$$\frac{\partial \mathbb{L}}{\partial \vartheta} = 0. \vartheta = \mathbb{U}_{\bar{m}\bar{n}}, \mathbb{V}_{\bar{m}\bar{n}}, \mathbb{W}_{\bar{m}\bar{n}} \quad (30)$$

By integrating Eqs. (22a), (22b), (22c) and (29) into Eq. (30), the motion equation of the composite structure can be achieved,

$$(\mathbf{k} - \omega^2 \mathbf{m}) \mathfrak{g} = 0. \quad (31)$$

where \mathbf{m} stands for the mass matrices associated with the kinetic energy; \mathbf{k} is the stiffness matrix associated with strain energy, potential energy contained in the boundaries, elastic foundation, and mechanical load; $\mathfrak{g} = [\mathfrak{g}_u, \mathfrak{g}_v, \mathfrak{g}_w]^T$ in which:

$$\mathbf{m} = \begin{bmatrix} \mathbf{m}_{uu} & 0 & 0 \\ 0 & \mathbf{m}_{vv} & 0 \\ 0 & 0 & \mathbf{m}_{ww} \end{bmatrix}, \quad (32a)$$

$$\begin{aligned} \mathbf{m}_{uu} &= \iint \int \rho r \mathbf{U}^T \mathbf{U} dV, \mathbf{m}_{vv} = \iint \int \rho r \mathbf{V}^T \mathbf{V} dV, \mathbf{m}_{ww} \\ &= \iint \int \rho r \mathbf{W}^T \mathbf{W} dV, \end{aligned} \quad (32b)$$

$$dV = r dr d\theta dx, \quad (32c)$$

where

$$\mathbf{V} = \mathbf{W} = \mathbf{U}, \quad (28b)$$

$$\mathfrak{g}_u = \{ \mathbb{U}_{00}^c, \dots, \mathbb{U}_{\bar{m}\bar{n}}^c, \dots, \mathbb{U}_{MN}^c, \mathbb{U}_{00}^s, \dots, \mathbb{U}_{\bar{m}\bar{n}}^s, \dots, \mathbb{U}_{MN}^s \} e^{i\omega t}, \quad (28c)$$

$$\mathfrak{g}_v = \{ \mathbb{V}_{00}^c, \dots, \mathbb{V}_{\bar{m}\bar{n}}^c, \dots, \mathbb{V}_{MN}^c, \mathbb{V}_{00}^s, \dots, \mathbb{V}_{\bar{m}\bar{n}}^s, \dots, \mathbb{V}_{MN}^s \} e^{i\omega t}, \quad (28d)$$

$$\mathbf{k} = \begin{bmatrix} \mathbf{k}_{uu} & \mathbf{k}_{uv} & \mathbf{k}_{uw} \\ \mathbf{k}_{uv}^T & \mathbf{k}_{vv} & \mathbf{k}_{vw} \\ \mathbf{k}_{uw}^T & \mathbf{k}_{vw}^T & \mathbf{k}_{ww} \end{bmatrix}, \quad (32d)$$

$$\begin{aligned} k_{uu} = & \iiint \left(Q_{11} r \frac{\partial U^T}{\partial x} \frac{\partial U}{\partial x} + Q_{55} r \frac{\partial U^T}{\partial r} \frac{\partial U}{\partial r} + Q_{66} \frac{1}{r} \frac{\partial U^T}{\partial \theta} \frac{\partial U}{\partial \theta} \right) dV \\ & + \iint \left\{ k_{u0} U^T U|_{x=0} + k_{uL} U^T U|_{x=L} \right\} dS_1, \end{aligned} \quad (32e)$$

$$k_{uv} = \iiint \left\{ Q_{12} \frac{\partial U^T}{\partial x} \frac{\partial V}{\partial \theta} + Q_{66} \frac{\partial U^T}{\partial \theta} \frac{\partial V}{\partial x} \right\} dV, \quad (32f)$$

$$k_{uw} = \iiint \left\{ Q_{12} \frac{\partial U^T}{\partial x} W + Q_{13} r \frac{\partial U^T}{\partial x} \frac{\partial W}{\partial r} + Q_{55} r \frac{\partial U^T}{\partial r} \frac{\partial W}{\partial r} \right\} dV, \quad (32g)$$

$$\begin{aligned} k_{vv} = & \iiint \left\{ \frac{Q_{22}}{r} \frac{\partial V^T}{\partial \theta} \frac{\partial V}{\partial \theta} + \frac{Q_{44}}{r} V^T V + Q_{44} r \frac{\partial V^T}{\partial r} \frac{\partial V}{\partial r} \right. \\ & \left. + Q_{66} r \frac{\partial V^T}{\partial x} \frac{\partial V}{\partial x} - Q_{44} \left(V^T \frac{\partial V}{\partial r} + \frac{\partial V^T}{\partial r} V \right) \right\} dV \\ & + \iint \left\{ k_{v0} V^T V|_{x=0} + k_{vL} V^T V|_{x=L} \right\} dS_1, \end{aligned} \quad (32h)$$

$$\begin{aligned} k_{vw} = & \iiint \left\{ \frac{Q_{22}}{r} \frac{\partial V^T}{\partial \theta} W + Q_{23} \frac{\partial V^T}{\partial \theta} \frac{\partial W}{\partial r} + Q_{44} \frac{\partial V^T}{\partial r} \frac{\partial W}{\partial \theta} \right. \\ & \left. - \frac{Q_{44}}{r} V^T \frac{\partial W}{\partial \theta} \right\} dV, \end{aligned} \quad (32i)$$

$$\begin{aligned} k_{ww} = & \iiint \left\{ \frac{Q_{22}}{r} W^T W + Q_{23} \left(W^T \frac{\partial W}{\partial r} + \frac{\partial W^T}{\partial r} W \right) \right. \\ & \left. + Q_{33} r \frac{\partial W^T}{\partial r} \frac{\partial W}{\partial r} + \frac{Q_{44}}{r} \frac{\partial W^T}{\partial \theta} \frac{\partial W}{\partial \theta} + Q_{55} r \frac{\partial W^T}{\partial x} \frac{\partial W}{\partial x} \right\} dV \\ & + \iint \left\{ k_{w0} W^T W|_{x=0} + k_{wL} W^T W|_{x=L} \right\} dS_1 \\ & + \iint \left\{ K_W W^T W + K_P \frac{\partial W^T}{\partial x} \frac{\partial W}{\partial x} + \frac{K_P}{r^2} \frac{\partial W^T}{\partial \theta} \frac{\partial W}{\partial \theta} \right\} |_{r=R_0} R_0 dS_3 \\ & + \iint \left\{ P \frac{\partial W^T}{\partial x} \frac{\partial W}{\partial x} + \frac{S}{r^2} \frac{\partial W^T}{\partial \theta} \frac{\partial W}{\partial \theta} \right\} |_{r=R_0} R_0 dS_3, \end{aligned} \quad (32j)$$

$$dS_1 = r dr d\theta, \quad dS_3 = dx d\theta, \quad (32k)$$

Also, the dimensionless parameters can be computed as follows:

$$K_W^* = \frac{K_W R^5}{E_m I}, \quad K_P^* = \frac{K_P R^3}{E_m I}, \quad P_0 = 1 \text{ [MPa]}. \quad (33)$$

3. Introducing artificial intelligence optimization technique to predict resonance frequency in advanced composite structures

The application of artificial intelligence (AI) in the field of material science, particularly in predicting the resonance

frequency of advanced composite structures, has gained significant traction due to its ability to analyze complex relationships and optimize parameters. This technique addresses challenges in traditional computational methods by leveraging AI-driven optimization for accurate predictions of resonance frequencies. This paper introduces a novel AI optimization framework designed to predict resonance frequency in composite structures efficiently. Advanced composite materials are widely used in aerospace, automotive, and civil engineering industries due to their high strength-to-weight ratios, durability, and design flexibility. However, predicting their resonance frequency, a critical property that affects the structural performance, remains a complex task. The resonance frequency is influenced by several factors, including material properties, geometric configurations, boundary conditions, and environmental factors. Traditional methods like finite element analysis (FEA) can be computationally expensive and time-consuming, especially for large or intricate composite structures. With the advancements in machine learning (ML) and optimization algorithms, AI offers new possibilities for improving predictive models' accuracy and efficiency. This paper explores how AI optimization techniques can be applied to predict the resonance frequency of composite structures with a focus on reducing computational time while maintaining high accuracy. Resonance frequency is a key dynamic property of a structure, representing the frequency at which it naturally tends to oscillate. For composite materials, factors such as anisotropy, non-homogeneous nature, and the presence of multiple layers make the prediction of resonance frequencies more challenging compared to traditional isotropic materials. Misestimating resonance frequencies can lead to catastrophic failures, particularly in structures subject to cyclic loading or dynamic stresses.

3.1. Limitations of conventional methods

The conventional approaches to predicting resonance frequencies involve:

- **Finite Element Analysis (FEA):** Accurate but computationally intensive, especially for complex composites.
- **Analytical Methods:** Limited to simpler geometries and material configurations.
- **Empirical Methods:** Dependent on past experimental data and limited in terms of generalization.

These methods struggle to handle the complexity and variability of advanced composites effectively and efficiently.

3.2. AI-based optimization techniques

AI-based optimization methods integrate predictive models with optimization algorithms to enhance accuracy and reduce computational load. Here are some key AI techniques that can be applied.

3.3. Machine learning (ML) models

ML models can be trained using data from previous simulations, experiments, or hybrid models combining both approaches. Some commonly used ML models in this domain include:

- **Neural Networks (NNs):** Can capture non-linear relationships between the variables affecting resonance frequency.
- **Support Vector Machines (SVM):** Used for regression tasks in predicting continuous variables like resonance frequencies.
- **Gaussian Processes (GP):** Provide probabilistic predictions and quantify uncertainty in the predictions.

3.4. Optimization algorithms

To optimize the parameters that influence resonance frequency predictions, AI-driven optimization techniques can be employed:

- **Genetic Algorithms (GA):** Mimics the process of natural selection to optimize the design variables of composite structures for accurate resonance frequency predictions.
- **Particle Swarm Optimization (PSO):** Uses a population-based search approach where candidate solutions (particles) are adjusted iteratively to converge on the optimal set of parameters.
- **Bayesian Optimization:** Works well with limited data by constructing a probabilistic model to optimize the parameters that affect resonance frequency.

3.5. Proposed AI-based optimization framework

The proposed AI-based optimization framework to predict resonance frequency in composite structures involves the following steps:

Step 1: Data acquisition

Gather experimental or simulated data related to material properties, geometric configurations, and boundary conditions affecting the resonance frequency. This dataset will serve as the foundation for training the AI model.

Step 2: Feature engineering

Select and preprocess the key features influencing resonance frequency, such as fiber orientation, layer thickness, matrix properties, boundary conditions, and load conditions. Dimensionality reduction techniques, like Principal Component Analysis (PCA), can be used to remove redundant features.

Step 3: Model training

Use supervised learning models like neural networks or support vector regression (SVR) to train the AI model on

the dataset. This model will learn the relationship between input features (material and structural parameters) and output (resonance frequency).

Step 4: Model validation and testing

Evaluate the trained model using cross-validation techniques to ensure generalization and minimize overfitting. The model's performance is assessed using metrics such as mean absolute error (MAE) or root mean squared error (RMSE).

Step 5: Optimization using AI algorithms

Apply an AI optimization algorithm (e.g. genetic algorithms or particle swarm optimization) to fine-tune the model parameters. This step ensures that the predicted resonance frequency is optimized for specific design requirements.

Step 6: Prediction

Once optimized, the AI model can predict resonance frequencies for new composite structures or configurations with high accuracy.

AI optimization techniques offer a powerful tool for predicting the resonance frequencies of advanced composite structures with greater efficiency and accuracy than conventional methods. By incorporating machine learning models and optimization algorithms, the proposed framework provides a flexible and scalable solution to complex dynamic problems in materials engineering. Future work will focus on expanding the dataset, refining the model's prediction accuracy, and integrating the framework into commercial software for practical use.

3.6. Mathematics simulation of the AI optimization technique

To simulate the AI optimization technique for predicting resonance frequency in composite structures, we can break it down into two main parts: Machine Learning for Prediction and Optimization Algorithm. The steps below outline a simple mathematical simulation that can be adapted into a more complex framework.

A simple Python code of the mentioned algorithm is given in Figure 3.

4. Numerical result

4.1. Validation of the results via a nondestructive testing

Figure 4 compares the natural frequencies of a cylindrical shell as a function of the number of circumferential waves. The x-axis represents the number of circumferential waves, while the y-axis shows the natural frequency, denoted as $\omega/2\pi$, in units of Hz. Two sets of data are presented: one is labeled "Present study" (depicted by a solid black line), and

```

import numpy as np
import pandas as pd
from sklearn.model_selection import train_test_split
from sklearn.preprocessing import StandardScaler
from sklearn.svm import SVC
from sklearn.datasets import load_iris
from sklearn.metrics import accuracy_score
# Load Iris dataset
iris = load_iris()
X = iris.data
y = iris.target
# Split into train and test sets
X_train, X_test, y_train, y_test = train_test_split(X, y,
test_size=0.3, random_state=42)
# Standardize the dataset
scaler = StandardScaler()
X_train = scaler.fit_transform(X_train)
X_test = scaler.transform(X_test)
# Particle Swarm Optimization (PSO) Parameters
n_particles = 30
n_iterations = 50
w = 0.5 # inertia weight
c1 = 2 # cognitive constant
c2 = 2 # social constant
bounds = {'C': (0.1, 1000), 'gamma': (0.0001, 1)} #
search space bounds for SVM parameters
# Initialize particles (random positions and velocities)
def initialize_particles():
    particles = []
    velocities = []
    for _ in range(n_particles):
        C = np.random.uniform(bounds['C'][0],
bounds['C'][1])
        gamma =
np.random.uniform(bounds['gamma'][0],
bounds['gamma'][1])
        velocity_C = np.random.uniform(-1, 1)
        velocity_gamma = np.random.uniform(-1, 1)
        particles.append([C, gamma])
        velocities.append([velocity_C, velocity_gamma])
    return np.array(particles), np.array(velocities)
# Fitness function: Negative accuracy (since we want
to minimize)
def fitness_function(particle):
    C, gamma = particle
    svm = SVC(C=C, gamma=gamma)
    svm.fit(X_train, y_train)
    y_pred = svm.predict(X_test)
    return -accuracy_score(y_test, y_pred)

# PSO Algorithm
def pso():
    # Initialize particles and velocities
    particles, velocities = initialize_particles()
    p_best = particles.copy() # personal best positions
    g_best = particles[np.argmin([fitness_function(p) for
p in particles])] # global best position
    for iteration in range(n_iterations):
        for i in range(n_particles):
            # Update velocities
            r1, r2 = np.random.rand(), np.random.rand()
            velocities[i] = (w * velocities[i] +
c1 * r1 * (p_best[i] - particles[i]) +
c2 * r2 * (g_best - particles[i]))
            # Update particles positions
            particles[i] = particles[i] + velocities[i]
            # Clip positions to be within bounds
            particles[i][0] = np.clip(particles[i][0],
bounds['C'][0], bounds['C'][1])
            particles[i][1] = np.clip(particles[i][1],
bounds['gamma'][0], bounds['gamma'][1])
            # Evaluate new fitness
            if fitness_function(particles[i]) <
fitness_function(p_best[i]):
                p_best[i] = particles[i] # update personal
best
            # Update global best
            g_best = p_best[np.argmin([fitness_function(p)
for p in p_best])]
            print(f"Iteration {iteration+1}/{n_iterations},
Best Fitness: {-fitness_function(g_best)}")
        return g_best
# Run PSO to optimize SVM hyperparameters
best_params = pso()
print(f"\nOptimized parameters (C, gamma):
{best_params}")
# Train final model with optimized parameters
svm_optimized = SVC(C=best_params[0],
gamma=best_params[1])
svm_optimized.fit(X_train, y_train)
y_pred_optimized = svm_optimized.predict(X_test)
accuracy_optimized = accuracy_score(y_test,
y_pred_optimized)
print(f"\nAccuracy with optimized parameters:
{accuracy_optimized:.4f}")

```

Figure 3. A simple Python code of the mentioned algorithm.

the other, “Experimental Sewall and Naumann [63]” (shown as red circles), indicating experimental results from a previous study by Sewall and Naumann [63]. The natural frequency decreases initially with an increasing number of circumferential waves, reaching a minimum at around six waves. After this point, it begins to rise again, showing a quadratic-like behavior for the remainder of the wave numbers. The shape of the curve suggests that the natural frequency is influenced by both the geometry and boundary conditions of the cylindrical shell, exhibiting a critical point at a certain number of circumferential waves before rising sharply. The figure also demonstrates the good agreement between the theoretical predictions of the present study and the experimental data from Sewall and Naumann [63]. While the trend in both data sets follows a similar pattern, there are some small deviations, particularly at higher wave

numbers (greater than 10 circumferential waves), where the experimental data slightly diverge from the theoretical curve. Overall, the graph highlights the effectiveness of the theoretical model in predicting the natural frequencies of the shell, while also validating the experimental data as a reference benchmark, showcasing the relationship between circumferential waves and the shell’s dynamic response.

4.2. Parametric results

Figure 5 presents the influence of nanoclay reinforcement on the dynamic behavior of a concrete cylindrical shell, particularly focusing on the changes in the relative frequency as a function of dimensionless applied pressure for various boundary conditions and geometric ratios. The three

subplots, each representing different boundary conditions—Simply-Simply, Clamped-Clamped, and Clamped-Free show the relative frequency change as a function of P^*/P_0 . The relative frequency change is expressed as $(\omega_n - \omega_w)/\omega_w$, where ω_n represents the natural frequency of the structure with nanoclay reinforcement, and ω_w is the natural frequency without nanoclay. In all plots, the relative frequency

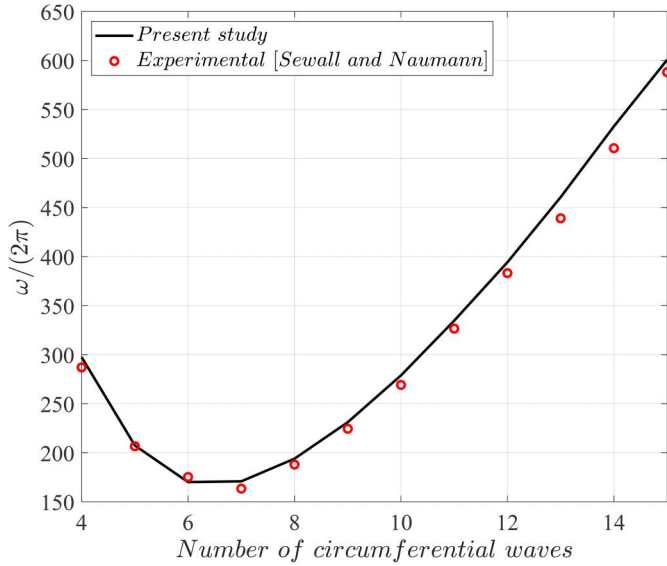


Figure 4. Comparison of the natural frequencies of cylindrical shell.

change increases with increasing dimensionless pressure P^*/P_0 , but the rate of increase and the magnitude of this change depend on the boundary conditions and the reinforcement ratios, denoted by $R/h = 30, 35,$ and 40 , which represent the ratios of the radius to the thickness of the cylindrical shell. For the Simply-Simply boundary condition (top left), the relative frequency change is gradual for lower P^*/P_0 values but rises steeply beyond $P^*/P_0 > 0.6$, with the $R/h = 40$ showing the most significant increase. This behavior indicates that as the shell experiences higher pressure, the nanoclay reinforcement more significantly influences the dynamic response, especially for thinner shells (larger R/h). In the Clamped-Clamped condition (top right), the increase in relative frequency change is less pronounced, particularly for $R/h = 30$, suggesting that clamped edges restrict the shell's deformation, limiting the effect of reinforcement. For Clamped-Free (bottom), the frequency change is generally higher compared to the clamped conditions. The Clamped-Free configuration, in particular, shows the largest frequency changes for all R/h values, demonstrating the significant impact of boundary flexibility on the effectiveness of nanoclay reinforcement. Overall, the figure illustrates that nanoclay reinforcement leads to a substantial improvement in the dynamic performance of the shell, particularly under higher pressures and in boundary conditions that allow greater deformation. The effect is more pronounced in shells with larger R/h values.

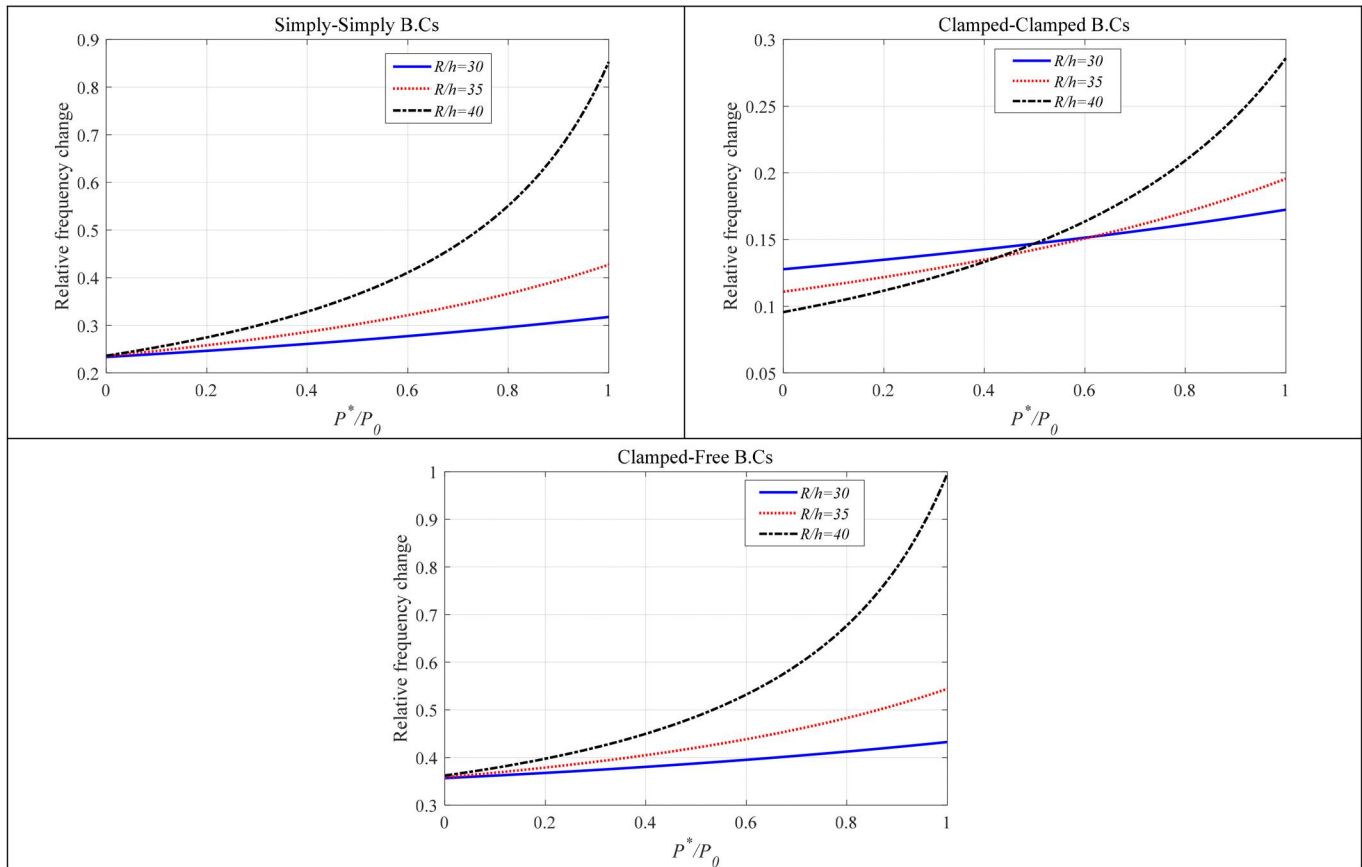


Figure 5. The influence of nanoclay reinforcement on the dynamic behavior of a concrete cylindrical shell, particularly focusing on the changes in the relative frequency as a function of dimensionless applied pressure for various boundary conditions and geometric ratios.

Figure 6 illustrates the variation of relative frequency change as a function of the dimensionless applied pressure for different values of the dimensionless Pasternak foundation coefficient. The three curves represent the system's behavior for $K_p^* = 0$ (blue solid line), $K_p^* = 1$ (red dotted line), and $K_p^* = 2$ (black dashed line). These values correspond to different levels of support provided by the elastic foundation modeled by the Pasternak parameter, which characterizes shear interactions in the foundation. The graph reveals a complex relationship between the relative frequency change and the applied pressure. Initially, for lower values of P^*/P_0 , the relative frequency change remains relatively constant across all K_p^* values, indicating that the effect of the Pasternak foundation on the natural frequency is negligible under low pressure. However, as the dimensionless pressure increases, distinct peaks emerge, signifying the occurrence of critical pressures where the system experiences abrupt changes in dynamic behavior. These critical pressures, marked by sharp increases in the relative frequency change, are highlighted in the figure with annotations. The blue curve for $K_p^* = 0$ shows a significant spike at around $P^*/P_0 = 1.5$, while the red and black curves for $K_p^* = 1$ and $K_p^* = 2$ exhibit peaks at higher pressure values, around $P^*/P_0 = 2$ and $P^*/P_0 = 2.5$, respectively. The presence of the foundation, particularly at higher K_p^* values, delays the onset of critical pressure, indicating that the foundation provides additional stability to the system. In conclusion, the figure demonstrates that the Pasternak foundation has a stabilizing effect on the cylindrical shell, increasing its resistance to dynamic instability at higher applied pressures. However, the system becomes highly sensitive at specific critical pressure points, where the relative frequency changes dramatically.

Figure 7 presents a relationship between the relative frequency change and the dimensionless applied pressure, considering various values of the dimensionless Winkler coefficient. The analysis is performed on a concrete cylindrical shell, reinforced by nanoclay, which serves as a critical component in bridge construction. The three distinct curves

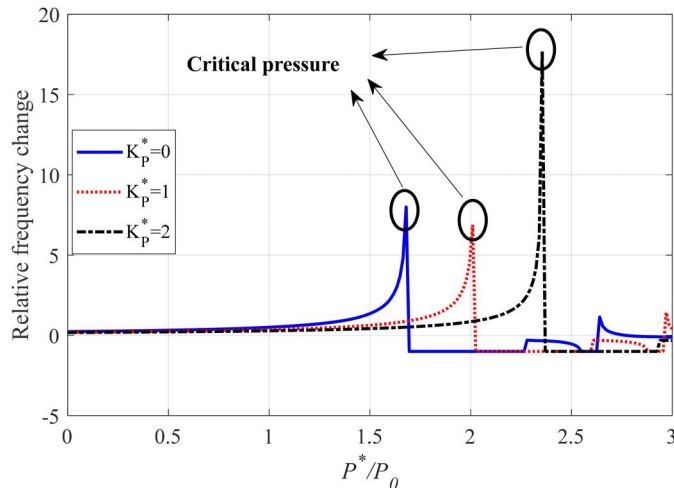


Figure 6. The variation of relative frequency change as a function of the dimensionless applied pressure for different values of the dimensionless Pasternak foundation coefficient.

in the plot correspond to different values of the Winkler coefficient: $K_W^* = 0$ (solid blue line), $K_W^* = 1$ (dotted red line), and $K_W^* = 2$ (dashed black line). These curves show how the relative frequency change increases as the dimensionless applied pressure rises, indicating a nonlinear trend where the effect of increasing pressure on the relative frequency becomes more pronounced, especially for higher values of K_W^* . The relative frequency change quantifies how the inclusion of nanoclay reinforcement (i.e., ω_n affects the natural frequency of the shell compared to the case without nanoclay ω_w). The results suggest that the higher the applied pressure and Winkler foundation stiffness, the larger the frequency change due to nanoclay reinforcement. For $K_W^* = 0$, where there is no Winkler foundation effect, the relative frequency change is highest, while for $K_W^* = 2$, it is lowest, suggesting that an increase in foundation stiffness dampens the effect of nanoclay reinforcement. This analysis highlights the significant role of foundation stiffness and applied pressure in tuning the vibrational behavior of nanoclay-reinforced cylindrical shells, which is crucial for designing durable and efficient structures like bridge components subjected to varying mechanical loads.

Figure 8 illustrates the relationship between the relative frequency change and the dimensionless applied pressure, as influenced by different weight fractions of nanoclay reinforcement in a concrete cylindrical shell. The figure depicts three curves for varying nanoclay weight fractions: $W_{NC} = 1\%$ (solid blue line), $W_{NC} = 2\%$ (dotted red line), and $W_{NC} = 3\%$ (dashed black line). As observed in the figure, the relative frequency change increases with both the applied pressure and the nanoclay weight fraction. The higher the nanoclay content, the greater the impact on the natural frequency of the shell. For a nanoclay weight fraction of $W_{NC} = 1\%$, the relative frequency change is lowest, exhibiting a more gradual increase as pressure rises. In contrast, when the nanoclay weight fraction is raised to $W_{NC} = 3\%$, the relative frequency change becomes significantly higher, showing a steeper increase for the same range of applied pressure. This trend demonstrates that as the nanoclay reinforcement content increases, the structural rigidity

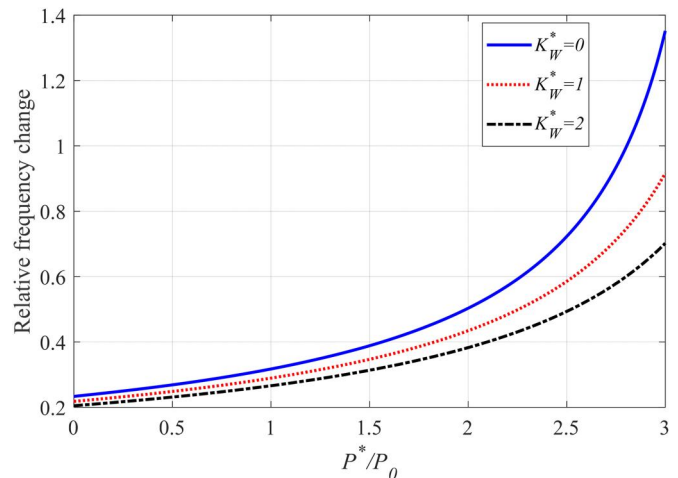


Figure 7. A relationship between the relative frequency change and the dimensionless applied pressure, considering various values of the dimensionless Winkler coefficient.

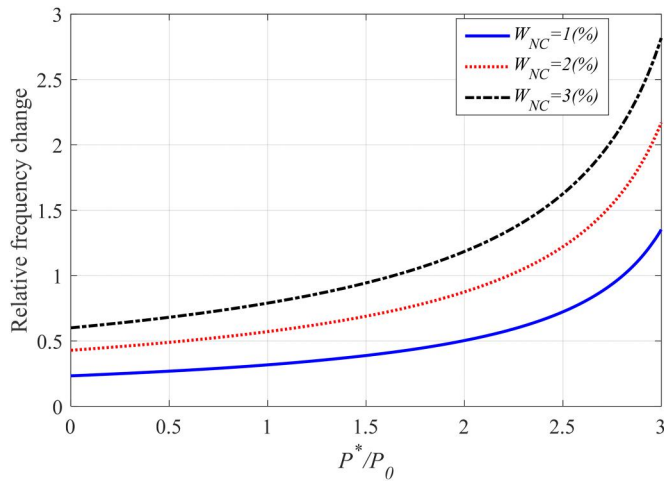


Figure 8. The relationship between the relative frequency change and the dimensionless applied pressure, as influenced by different weight fractions of nanoclay reinforcement in a concrete cylindrical shell.

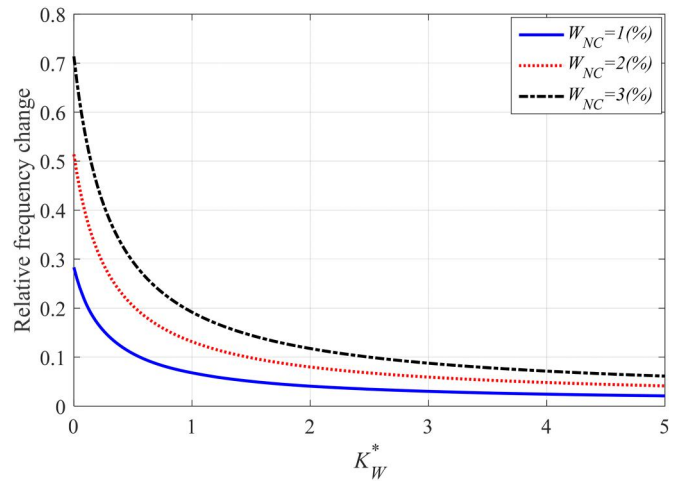


Figure 10. The relative frequency change of a cylindrical shell reinforced with nanoclay as a function of the dimensionless Winkler coefficient, for different weight fractions of nanoclay reinforcement.

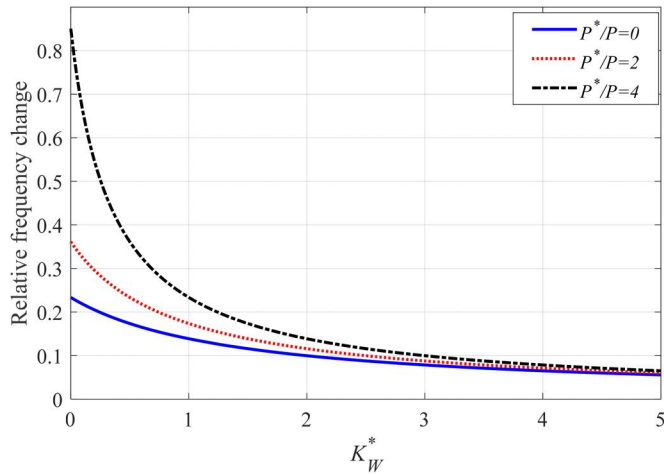


Figure 9. The relationship between the relative frequency change and the dimensionless Winkler coefficient, for different values of the dimensionless applied pressure.

and natural frequency of the shell improve, resulting in a more pronounced change in frequency under increasing pressure. The nonlinear behavior of the curves indicates that the influence of the applied pressure becomes stronger as nanoclay content grows, reflecting its stiffening effect on the material properties of the shell. This analysis is particularly relevant in the context of optimizing material reinforcement in bridge construction, where nanoclay reinforcement can be strategically used to enhance the vibrational performance of concrete cylindrical shells under varying load conditions.

Figure 9 displays the relationship between the relative frequency change and the dimensionless Winkler coefficient, for different values of the dimensionless applied pressure. The plot includes three curves representing different applied pressures: $P^*/P_0 = 0$ (solid blue line), $P^*/P_0 = 2$ (dotted red line), and $P^*/P_0 = 4$ (dashed black line). As seen in the graph, the relative frequency change decreases as the dimensionless Winkler coefficient increases, regardless of the applied pressure. The relative frequency change is highest when K_W^* is small, indicating that the impact of nanoclay reinforcement on the natural frequency is most significant

in systems with lower foundation stiffness. As K_W^* increases, the relative frequency change diminishes, converging toward a minimal value for higher Winkler coefficients. The effect of the applied pressure on the relative frequency change is also evident. For $P^*/P_0 = 0$, the relative frequency change is lowest across all K_W^* values. As the pressure increases to $P^*/P_0 = 4$, the relative frequency change becomes larger, indicating that higher applied pressure amplifies the frequency shift due to nanoclay reinforcement. However, the rate of decrease with respect to K_W^* remains consistent across different pressures, suggesting that the influence of the Winkler foundation stiffening effect is dominant at higher K_W^* values. This figure highlights the interaction between foundation stiffness and applied pressure in determining the vibrational behavior of nanoclay-reinforced cylindrical shells. It underscores the fact that while applied pressure enhances the frequency change, the Winkler coefficient moderates this effect by stiffening the foundation, leading to a reduced relative frequency change as K_W^* grows.

Figure 10 illustrates the relative frequency change of a cylindrical shell reinforced with nanoclay as a function of the dimensionless Winkler coefficient, for different weight fractions of nanoclay reinforcement. Three curves are shown corresponding to different weight fractions of nanoclay: 1%, 2%, and 3%, represented by the blue solid line, red dotted line, and black dashed line, respectively. The trend reveals that the relative frequency change decreases with increasing K_W^* for all nanoclay weight fractions. This behavior indicates that, as the Winkler foundation's stiffness increases, the influence of the nanoclay reinforcement on the natural frequency becomes less pronounced. At smaller values of K_W^* , the relative frequency change is more significant, especially for higher nanoclay content. For $W_{NC} = 3\%$, the relative frequency change reaches approximately 0.7 for very small K_W^* , indicating a substantial increase in the natural frequency due to nanoclay reinforcement. In contrast, for $W_{NC} = 1\%$, the relative frequency change is lower, showing that the frequency enhancement is less prominent for smaller amounts of reinforcement. As K_W^* increases toward 5, the relative frequency change approaches a plateau for all

curves, suggesting that further increases in foundation stiffness provide diminishing returns in terms of frequency enhancement from nanoclay reinforcement. The figure thus highlights the combined effects of nanoclay reinforcement and foundation stiffness on the dynamic response of cylindrical shells in bridge construction.

Figure 11 shows the relative frequency change of a cylindrical shell reinforced with nanoclay under different values of the dimensionless Pasternak coefficient, as a function of the dimensionless Winkler coefficient. Three curves represent different values of the Pasternak coefficient: $K_p^* = 0$, $K_p^* = 1$, and $K_p^* = 2$, corresponding to the blue solid line, red dotted line, and black dashed line, respectively. The graph demonstrates how both the Pasternak and Winkler foundation coefficients influence the dynamic behavior of the shell structure. The general trend across all three curves is a reduction in the relative frequency change as the dimensionless Winkler coefficient, K_w^* , increases. This decrease indicates that, as the Winkler foundation's stiffness increases, the relative impact of the nanoclay reinforcement on the natural frequency diminishes. For $K_p^* = 0$, the relative frequency change is highest, peaking at around 0.09 for small K_w^* . As the Pasternak coefficient increases to $K_p^* = 1$ and $K_p^* = 2$, the relative frequency change decreases, showing that the Pasternak foundation adds additional stiffness to the system, reducing the frequency change induced by the nanoclay reinforcement. At large values of K_w^* , the curves approach a steady state, indicating a negligible influence of the Winkler coefficient as both K_w^* and K_p^* increase. Overall, this figure emphasizes the interplay between the Winkler and Pasternak foundation parameters and the effectiveness of nanoclay reinforcement in modifying the shell's natural frequency.

Figure 12 presents the relationship between the relative frequency change of a concrete cylindrical shell, reinforced with nanoclay, and the ratio of the shell's radius to its thickness. The relative frequency change is a measure of how sensitive the natural frequency of the shell is to the presence of nanoclay reinforcement. The plot displays three different cases based on the dimensionless applied pressure ratio, which is a critical parameter in analyzing the structural response of the shell under

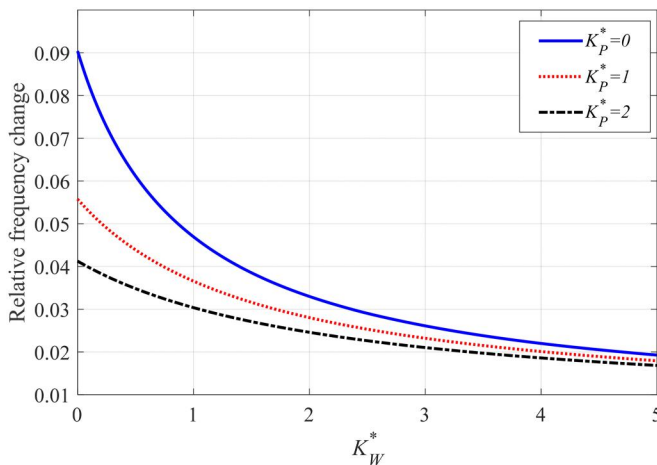


Figure 11. The relative frequency change of a cylindrical shell reinforced with nanoclay under different values of the dimensionless Pasternak coefficient, as a function of the dimensionless Winkler coefficient.

varying pressure conditions. The blue solid line represents the scenario where $P^*/P_0 = 0$, indicating no applied external pressure. The red dotted line corresponds to $P^*/P_0 = 0.1$, while the black dashed line corresponds to $P^*/P_0 = 0.2$. These lines illustrate that as the dimensionless applied pressure increases, the relative frequency change also increases, showing that the frequency becomes more sensitive to the presence of nanoclay under higher pressures. The x-axis of the graph represents the ratio R/h , which ranges from 20 to 50. As this ratio increases, indicating a thinner shell relative to its radius, the relative frequency change increases nonlinearly for all three pressure conditions. This nonlinear trend suggests that shells with a higher R/h ratio are more influenced by nanoclay reinforcement, particularly under higher applied pressures. The figure thus highlights the importance of considering both the dimensionless applied pressure and the R/h ratio when evaluating the sensitivity of a nanoclay-reinforced concrete cylindrical shell, as these factors significantly impact the structural performance and frequency behavior.

Figure 13 illustrates the relationship between the relative frequency change of a concrete cylindrical shell reinforced

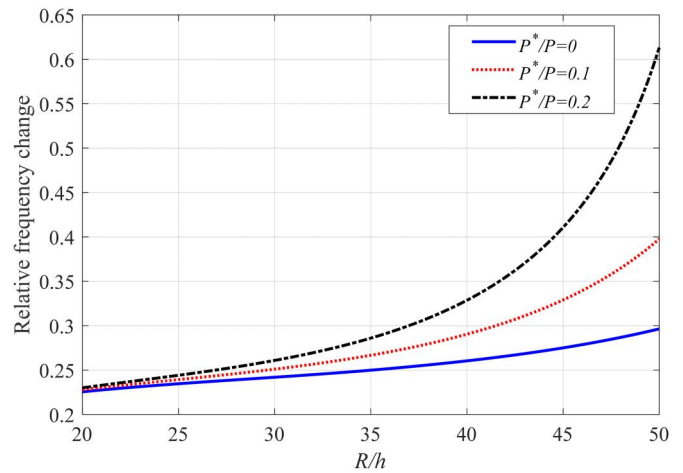


Figure 12. The relationship between the relative frequency change of a concrete cylindrical shell, reinforced with nanoclay, and the ratio of the shell's radius to its thickness.

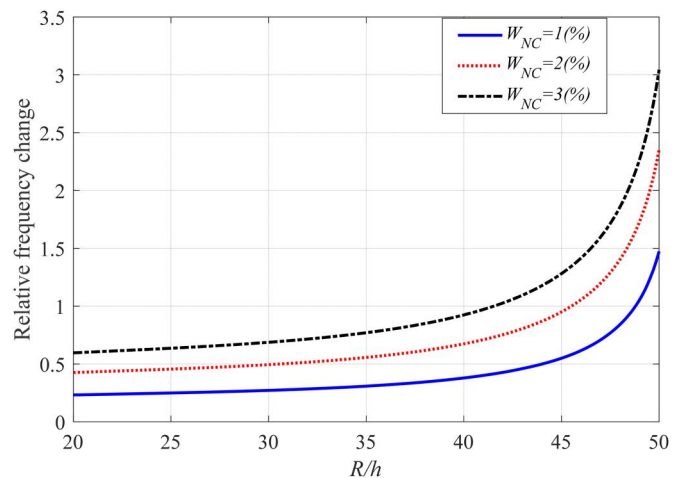


Figure 13. The relationship between the relative frequency change of a concrete cylindrical shell reinforced with nanoclay and the ratio of the shell's radius to its thickness.

with nanoclay and the ratio of the shell's radius to its thickness. The focus of this graph is on how different weight fractions of nanoclay reinforcement W_{NC} affect the frequency sensitivity of the shell structure. The x-axis represents the R/h ratio, varying from 20 to 50, while the y-axis shows the relative frequency change. Three distinct lines represent different weight fractions of nanoclay. The blue solid line corresponds to $W_{NC} = 1\%$. The red dotted line corresponds to $W_{NC} = 2\%$. The black dashed line corresponds to $W_{NC} = 3\%$. As the R/h ratio increases, the relative frequency change increases for all three cases. This trend indicates that as the shell becomes thinner relative to its radius, it becomes more sensitive to the reinforcement provided by the nanoclay. The degree of sensitivity is higher for larger weight fractions of nanoclay, as evident from the steeper curves for $W_{NC} = 3\%$ and $W_{NC} = 2\%$, compared to $W_{NC} = 1\%$. This graph suggests that increasing the nanoclay content enhances the stiffness and consequently the frequency of the shell, particularly as the shell becomes thinner (higher R/h). The nonlinear increase in the relative frequency change with both the R/h ratio and W_{NC} highlights the critical role of nanoclay reinforcement in influencing the dynamic behavior of the cylindrical shell structure. Thus, higher nanoclay content leads to greater improvements in the shell's frequency response, making it more resilient under dynamic loading conditions.

Figure 14 is a three-dimensional surface plot that illustrates the relationship between the relative frequency change of a concrete cylindrical shell reinforced with nanoclay and two key dimensionless parameters: Pasternak coefficient and applied pressure. The x-axis represents the dimensionless Pasternak coefficient, which is related to the shear interaction in the foundation. The y-axis represents the dimensionless applied pressure, which is a measure of the external pressure applied to the shell relative to a reference pressure. The z-axis represents the relative frequency change, which indicates the sensitivity of the shell's natural frequency to these two parameters. The surface plot shows that the relative frequency change is affected by both K_p^* and P^*/P_0 . For lower values of P^*/P_0 and K_p^* , the relative frequency change remains relatively small, indicating that the shell's frequency

is less sensitive to the nanoclay reinforcement under these conditions. However, as either P^*/P_0 or K_p^* increases, the relative frequency change becomes more pronounced, particularly when both parameters are near their higher values. The surface has a curved shape, indicating a nonlinear relationship between these variables. The increase in relative frequency change is more significant when both K_p^* and P^*/P_0 are large, suggesting that the combined effect of higher shear interaction in the foundation and higher applied pressure amplifies the sensitivity of the shell's frequency to the nanoclay reinforcement. This figure emphasizes the importance of considering both the foundation's shear characteristics and the applied pressure when analyzing the dynamic behavior of nanoclay-reinforced concrete cylindrical shells. These factors interact in a complex way to influence the structural performance, with significant implications for the design and analysis of such systems in engineering applications.

The link between the relative frequency change of a concrete cylindrical shell reinforced with nanoclay and two important dimensionless parameters—the Winkler coefficient and the applied pressure—is shown in Figure 15, a three-dimensional surface plot. The dimensionless Winkler coefficient, associated with the shear interaction in the foundation, is shown by the x-axis. The dimensionless applied pressure, which is a measurement of the external pressure applied to the shell in relation to a reference pressure, is shown by the y-axis. The relative frequency change, shown by the z-axis, shows how sensitive the natural frequency of the shell is to these two factors. The surface plot indicates that both K_w^* and P^*/P_0 have an impact on the relative frequency change. The relative frequency shift is still rather minor for lower levels of P^*/P_0 and K_w^* , suggesting that the shell's frequency is less susceptible to the nanoclay reinforcement in these circumstances. Nevertheless, the relative frequency change intensifies with increasing P^*/P_0 or K_w^* , especially when both parameters are close to their higher values. The curved form of the surface suggests that there is a nonlinear connection between these factors. When both K_w^* and P^*/P_0 are large, the relative frequency change increases more significantly, indicating that the higher shear

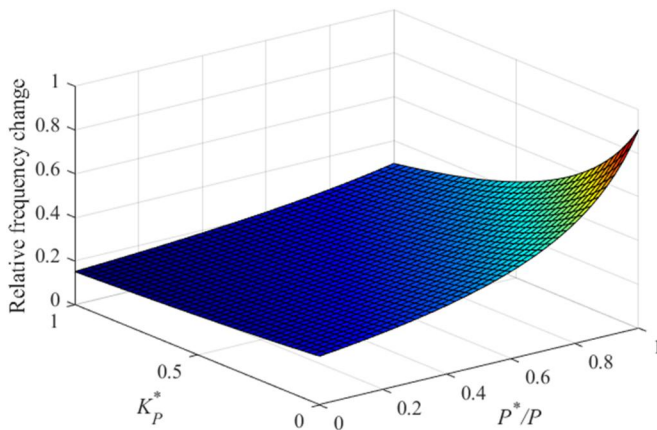


Figure 14. A three-dimensional surface plot that illustrates the relationship between the relative frequency change of a concrete cylindrical shell reinforced with nanoclay and two key dimensionless parameters.

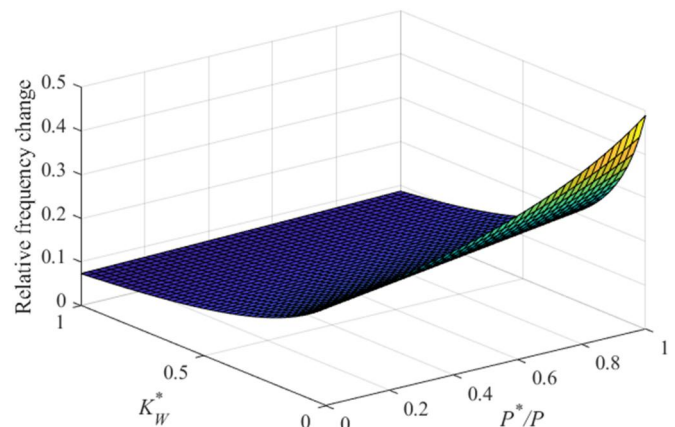


Figure 15. The relative frequency change of a concrete cylindrical shell reinforced with nanoclay and two important dimensionless parameters (Winkler coefficient and the applied pressure).

interaction in the foundation and the higher applied pressure together enhance the sensitivity of the shell's frequency to the nanoclay reinforcement. This image highlights how crucial it is to take into account the properties of the foundation as well as the applied pressure when examining the dynamic behavior of cylindrical shells of nanoclay-reinforced concrete. The intricate interplay of these variables affects the structural performance and has important ramifications for the engineering applications' design and analysis of such systems.

4.3. AI optimization algorithm results

The algorithm would now optimize over the resonance frequency by adjusting parameters such as the material and geometric properties listed above. The objective function to minimize would be the difference between the predicted and target resonance frequencies.

Figure 16 illustrates the loss factor plotted against epochs for both the training and testing datasets in the context of an AI optimization algorithm. The loss factor typically represents the error or cost function that the optimization process is trying to minimize. The blue curve corresponds to the training dataset, while the red curve represents the testing dataset. Initially, both curves show a high loss factor, which rapidly decreases during the early epochs. This suggests that the model is learning effectively, as both the training and testing errors are decreasing. The training curve exhibits a smoother decline, indicating stable learning, while the testing curve shows more fluctuations, which is expected due to the inherent variability in the testing set. As the number of epochs increases, the loss factor for the training dataset stabilizes at a lower value, signifying convergence of the learning process. The testing dataset also exhibits a gradual decrease in loss factor but with persistent fluctuations. These fluctuations might indicate slight overfitting or the inherent noise in the testing dataset. The convergence of both curves toward lower values suggests that the

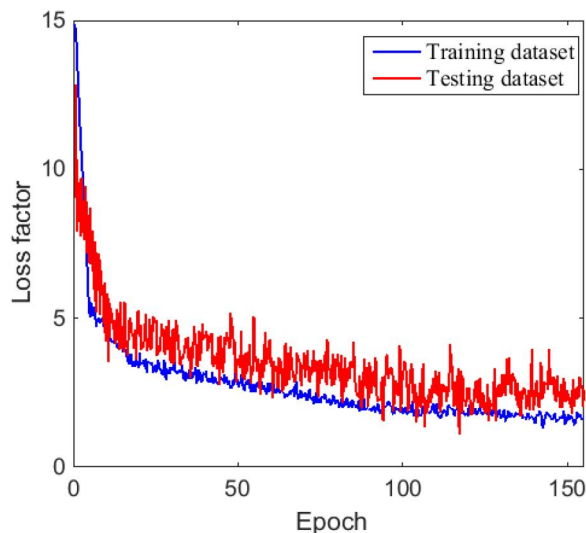


Figure 16. Loss factor against epoch for testing and training dataset for the mentioned AI optimization algorithm.

Table 2. DNN model's dimensionless frequency for varying RMSE and a/b values.

P^*/P_0	MR	Predicted		
		$RMSE_{Train} = 0.2359$	$RMSE_{Train} = 0.2591$	$RMSE_{Train} = 0.2891$
0	1.45359	1.12257	1.38457	1.45543
0.1	1.22202	1.00133	1.12046	1.22201
0.2	0.82305	0.56226	0.71699	0.82396
0.3	0.52731	0.43799	0.491	0.52906
0.4	0.28737	0.18366	0.27506	0.28724

Table 3. The DNN model's performance for dimensionless frequency for different R^2 and W_{GOP} .

$W_{NC}(wt\%)$	MR	Predicted		
		$R^2 = 0.9362$	$R^2 = 0.9651$	$R^2 = 0.9961$
0	0.71424	0.52877	0.66919	0.71587
1	1.02672	0.71699	0.87964	1.02556
2	1.11879	0.84126	1.04659	1.11866
3	1.63215	1.17622	1.39119	1.6333
4	1.95858	1.49819	1.86082	1.96003

optimization algorithm is effective, but the higher volatility in the testing curve warrants further investigation to ensure generalization without overfitting.

This section examines the effects of R^2 and RMSE on the results shown in Tables 2 and 3. It has been noted that responses with higher RMSE and R^2 values are more accurate. It is thus recommended to use $R^2 = 0.9961$, $RMSE = 0.2891$, and 4850 samples when selecting the findings. The findings of the mathematical modeling are also shown in mathematics results (MR).

Tables 2 and 3 show how the dimensionless deflection of the existing structure varies with W_{NC} and P^*/P_0 . Further details on this topic are provided in the section that follows.

5. Conclusion

In this study, the optimization and mathematical simulation of resonance frequency in nanoclay-reinforced concrete cylindrical shell structures, intended for bridge applications, were rigorously validated through nondestructive testing methods. The research demonstrated that incorporating nanoclay into the concrete mix significantly enhanced the material's mechanical properties, including stiffness and durability, which are crucial for maintaining structural integrity and longevity in bridge components. Mathematical simulations provided a comprehensive framework for predicting the resonance frequencies of the cylindrical shell structures, considering various factors such as material composition, geometric parameters, and load conditions. These simulations were optimized to identify the best possible performance for the nanoclay-reinforced concrete structures, minimizing vibrational issues that could compromise safety and functionality. Nondestructive testing, including frequency response analysis, were employed to validate the simulation results. The experimental data confirmed that the resonance frequencies of the test samples were consistent with the predicted values from the simulations. This validation emphasized the accuracy and reliability of the mathematical models used in the study. The research highlighted

the effectiveness of combining mathematical simulations with experimental validation through NDT to optimize the performance of nanoclay-reinforced concrete structures in bridge applications. The successful alignment between simulated and empirical results underscored the potential of this approach for designing more resilient and efficient bridge structures. The study suggested that such optimization techniques and advanced materials could significantly enhance infrastructure performance and longevity. Looking forward, future research should focus on expanding the scope of simulations to include additional variables and real-world conditions. This would further refine the design process and contribute to the development of more sustainable and durable bridge infrastructure, building on the successful validation achieved in this study.

Disclosure statement

No potential competing interest was reported by the authors.

Funding

This work was supported by Sichuan Province Luzhou city of Stars science and technology planning project (2022-GYF-6) and (2021-JYJ-95). The authors extend their appreciation to King Saud University, Saudi Arabia for funding this work through Researchers Supporting Project number (RSP2024R305), King Saud University, Riyadh, Saudi Arabia.

References

- [1] R. Augello, and E. Carrera, Analysis of plate reinforced by straight and curved stiffeners by using novel plate elements with refined through-the-thickness expansion, *Mech. Adv. Mater. Struct.*, vol. 31, no. 1, pp. 13–21, 2024. DOI: [10.1080/15376494.2023.2270794](https://doi.org/10.1080/15376494.2023.2270794).
- [2] E. Carrera, F. Miglioretti, and M. Petrolo, Accuracy of refined finite elements for laminated plate analysis, *Compos. Struct.*, vol. 93, no. 5, pp. 1311–1327, 2011. DOI: [10.1016/j.compstruct.2010.11.007](https://doi.org/10.1016/j.compstruct.2010.11.007).
- [3] M.R. Barati, and A.M. Zenkour, Vibration analysis of functionally graded graphene platelet reinforced cylindrical shells with different porosity distributions, *Mech. Adv. Mater. Struct.*, vol. 26, no. 18, pp. 1580–1588, 2019. DOI: [10.1080/15376494.2018.1444235](https://doi.org/10.1080/15376494.2018.1444235).
- [4] U. Caliskan, H. Gulsen, and M.K. Apalak, New approach for modeling randomly distributed CNT reinforced polymer nanocomposite with van Der Waals interactions, *Mech. Adv. Mater. Struct.*, vol. 31, no. 1, pp. 218–229, 2024. DOI: [10.1080/15376494.2023.2231443](https://doi.org/10.1080/15376494.2023.2231443).
- [5] Z. Li, W. Ma, H. Zhu, G. Deng, L. Hou, P. Xu, and S. Yao, Energy absorption prediction and optimization of corrugation-reinforced multicell square tubes based on machine learning, *Mech. Adv. Mater. Struct.*, vol. 29, no. 26, pp. 5511–5529, 2022. DOI: [10.1080/15376494.2021.1958032](https://doi.org/10.1080/15376494.2021.1958032).
- [6] G. Zhang, L. Tang, Z. Liu, L. Zhou, Y. Liu, and Z. Jiang, Machine-learning-based damage identification methods with features derived from moving principal component analysis, *Mech. Adv. Mater. Struct.*, vol. 27, no. 21, pp. 1789–1802, 2020. DOI: [10.1080/15376494.2019.1710308](https://doi.org/10.1080/15376494.2019.1710308).
- [7] Y. Lin, and A.A. Ibraheem, Machine learning method as a tool to estimate the vibrations of the concrete structures reinforced by advanced nanocomposites, *Mech. Adv. Mater. Struct.*, pp. 1–17, 2024. DOI: [10.1080/15376494.2024.2355517](https://doi.org/10.1080/15376494.2024.2355517).
- [8] T.-T. Le, Practical machine learning-based prediction model for axial capacity of square CFST columns, *Mech. Adv. Mater. Struct.*, vol. 29, no. 12, pp. 1782–1797, 2022. DOI: [10.1080/15376494.2020.1839608](https://doi.org/10.1080/15376494.2020.1839608).
- [9] J. Chen, J. Zhang, and H. Zhao, Quantifying alignment deviations for uniaxial material mechanical testing via automated machine learning, *Mech. Adv. Mater. Struct.*, pp. 1–14, 2022. DOI: [10.1080/15376494.2022.2128122](https://doi.org/10.1080/15376494.2022.2128122).
- [10] L.L. Vignoli, J. Gomide, L.E. Santana, Y.S. Macedo, and J.S. Oliveira, Using asymptotic homogenization and machine learning to derive a 3D Trace theory for GFRP, *Mech. Adv. Mater. Struct.*, pp. 1–13, 2024. DOI: [10.1080/15376494.2024.2326994](https://doi.org/10.1080/15376494.2024.2326994).
- [11] X. Zhou, Y. Chen, and M. Abbas, Transient bending analysis of the graphene nanoplatelets reinforced sandwich concrete building structure validated by machine learning algorithm, *Mech. Adv. Mater. Struct.*, pp. 1–22, 2024. DOI: [10.1080/15376494.2024.2344188](https://doi.org/10.1080/15376494.2024.2344188).
- [12] B.P. Koya, S. Aneja, R. Gupta, and C. Valeo, Comparative analysis of different machine learning algorithms to predict mechanical properties of concrete, *Mech. Adv. Mater. Struct.*, vol. 29, no. 25, pp. 4032–4043, 2022. DOI: [10.1080/15376494.2021.1917021](https://doi.org/10.1080/15376494.2021.1917021).
- [13] S.A. Chowdhury, C. Nelon, S. Li, O. Myers, and A. Hall, Quantification of the out-of-plane loading fatigue response of bistable CFRP laminates using a machine learning approach, *Mech. Adv. Mater. Struct.*, pp. 1–16, 2024. DOI: [10.1080/15376494.2024.2342027](https://doi.org/10.1080/15376494.2024.2342027).
- [14] C. Zhu, Intelligent robot path planning and navigation based on reinforcement learning and adaptive control, *J. Logistic Inform Service Sci.*, vol. 10, no. 3, pp. 235–248, 2023.
- [15] H. Huang, Z. Chen, M. Zhao, B. Wang, and Y. Ye, Seismic performance of frame with middle partially encased composite brace and steel-hollow core partially encased composite spliced frame beam, *J. Building Eng.*, pp. 110226, 2024. DOI: [10.1016/j.jobe.2024.110226](https://doi.org/10.1016/j.jobe.2024.110226).
- [16] A. Tariq, B. Uzun, B. Deliktaş, and M.Ö. Yaylı, Vibration analysis of embedded porous nanobeams under thermal effects using boosting machine learning algorithms and semi-analytical approach, *Mech. Adv. Mater. Struct.*, pp. 1–24, 2024. DOI: [10.1080/15376494.2024.2320809](https://doi.org/10.1080/15376494.2024.2320809).
- [17] S. Derogar, C. Ince, H.Y. Yatbaz, and E. Ever, Prediction of punching shear strength of slab-column connections: a comprehensive evaluation of machine learning and deep learning based approaches, *Mech. Adv. Mater. Struct.*, vol. 31, no. 6, pp. 1272–1290, 2024. DOI: [10.1080/15376494.2022.2134950](https://doi.org/10.1080/15376494.2022.2134950).
- [18] E. Carrera, M. Petrolo, M.H. Nagaraj, and M. Delicata, Evaluation of the influence of voids on 3D representative volume elements of fiber-reinforced polymer composites using CUF micromechanics, *Compos. Struct.*, vol. 254, pp. 112833, 2020. DOI: [10.1016/j.compstruct.2020.112833](https://doi.org/10.1016/j.compstruct.2020.112833).
- [19] E. Carrera, and V.V. Zozulya, Carrera unified formulation (CUF) for the micropolar beams: analytical solutions, *Mech. Adv. Mater. Struct.*, vol. 28, no. 6, pp. 583–607, 2021. DOI: [10.1080/15376494.2019.1578013](https://doi.org/10.1080/15376494.2019.1578013).
- [20] E. Carrera, R. Augello, A. Pagani, and D. Scano, Refined multi-layered beam, plate and shell elements based on Jacobi polynomials, *Compos. Struct.*, vol. 304, pp. 116275, 2023. DOI: [10.1016/j.compstruct.2022.116275](https://doi.org/10.1016/j.compstruct.2022.116275).
- [21] H. Wang, Y. Hou, Y. He, C. Wen, B. Giron-Palomares, Y. Duan, B. Gao, V.P. Vavilov, and Y. Wang, A physical-constrained decomposition method of infrared thermography: pseudo restored heat flux approach based on ensemble bayesian variance tensor fraction, *IEEE Trans. Ind. Informat.*, 2023. DOI: [10.1109/TII.2023.3293863](https://doi.org/10.1109/TII.2023.3293863).
- [22] Q. Wu, S. Wang, M. Yao, Y. Niu, and C. Wang, Nonlinear dynamics of three-layer microplates: simultaneous presence of the micro-scale and imperfect effects, *Eur Phys. J Plus.*, vol. 139, no. 5, pp. 1–21, 2024. DOI: [10.1140/epjp/s13360-024-05255-3](https://doi.org/10.1140/epjp/s13360-024-05255-3).
- [23] H. Kordestani, C. Zhang, and A. Arab, An investigation into the application of acceleration responses' trendline for bridge

- damage detection using quadratic regression, *Sensors.*, vol. 24, no. 2, pp. 410, 2024. DOI: [10.3390/s24020410](https://doi.org/10.3390/s24020410).
- [24] M. Li, T. Wang, F. Chu, Q. Han, Z. Qin, and M.J. Zuo, Scaling-basis Chirplet transform, *IEEE Trans. Indus. Electron.*, vol. 68, no. 9, pp. 8777–8788, 2020. DOI: [10.1109/TIE.2020.3013537](https://doi.org/10.1109/TIE.2020.3013537).
- [25] D. Lu, X. Zhou, X. Du, and G. Wang, 3D dynamic elastoplastic constitutive model of concrete within the framework of rate-dependent consistency condition, *J. Eng. Mech.*, vol. 146, no. 11, pp. 04020124, 2020. DOI: [10.1061/\(ASCE\)EM.1943-7889.0001854](https://doi.org/10.1061/(ASCE)EM.1943-7889.0001854).
- [26] X. Zhou, D. Lu, X. Du, G. Wang, and F. Meng, A 3D non-orthogonal plastic damage model for concrete, *Comput. Method. Appl. Mech. Eng.*, vol. 360, pp. 112716, 2020. DOI: [10.1016/j.cma.2019.112716](https://doi.org/10.1016/j.cma.2019.112716).
- [27] J. Cao, J. Du, Q. Fan, J. Yang, C. Bao, and Y. Liu, Reinforcement for earthquake-damaged glued-laminated timber knee-braced frames with self-tapping screws and CFRP fabric, *Eng. Struct.*, vol. 306, pp. 117787, 2024. DOI: [10.1016/j.engstruct.2024.117787](https://doi.org/10.1016/j.engstruct.2024.117787).
- [28] W. Zhang, D. Zheng, Y. Huang, and S. Kang, Experimental and simulative analysis of flexural performance in UHPC-RC hybrid beams, *Construct. Build Mater.*, vol. 436, pp. 136889, 2024. DOI: [10.1016/j.conbuildmat.2024.136889](https://doi.org/10.1016/j.conbuildmat.2024.136889).
- [29] H. Huang, C. Xue, W. Zhang, and M. Guo, Torsion design of CFRP-CFST columns using a data-driven optimization approach, *Eng. Struct.*, vol. 251, pp. 113479, 2022. DOI: [10.1016/j.engstruct.2021.113479](https://doi.org/10.1016/j.engstruct.2021.113479).
- [30] J. Wang, S.-Q. Lin, D.-Y. Tan, J.-H. Yin, H.-H. Zhu, and S.C. Kuok, A novel method for integrity assessment of soil-nailing works with actively heated fiber-optic sensors, *J. Geotech Geoenviron Eng.*, vol. 150, no. 8, pp. 04024063, 2024. DOI: [10.1061/JGGEFK.GTENG-11790](https://doi.org/10.1061/JGGEFK.GTENG-11790).
- [31] Y. Yang, B. Lin, and W. Zhang, Experimental and numerical investigation of an arch-beam joint for an arch bridge, *Arch. Civil Mech. Eng.*, vol. 23, no. 2, pp. 101, 2023d. DOI: [10.1007/s43452-023-00645-3](https://doi.org/10.1007/s43452-023-00645-3).
- [32] C. Zhang, The active rotary inertia driver system for flutter vibration control of bridges and various promising applications, *Science China Technol. Sci.*, vol. 66, no. 2, pp. 390–405, 2023. DOI: [10.1007/s11431-022-2228-0](https://doi.org/10.1007/s11431-022-2228-0).
- [33] H. Huang, Y. Yao, C. Liang, and Y. Ye, Experimental study on cyclic performance of steel-hollow core partially encased composite spliced frame beam, *Soil Dynam Earthq Eng.*, vol. 163, pp. 107499, 2022. DOI: [10.1016/j.soildyn.2022.107499](https://doi.org/10.1016/j.soildyn.2022.107499).
- [34] Y. Yao, L. Zhou, H. Huang, Z. Chen, and Y. Ye, Cyclic performance of novel composite beam-to-column connections with reduced beam section fuse elements, vol. 50, pp. 842–858, 2023. DOI: [10.1016/j.jstruct.2023.02.054](https://doi.org/10.1016/j.jstruct.2023.02.054).
- [35] B. Liu, H. Yang, and S. Karekal, Effect of water content on argillization of mudstone during the tunnelling process, *Rock Mech. Rock Eng.*, vol. 53, pp. 799–813, 2020. DOI: [10.1007/s00603-019-01947-w](https://doi.org/10.1007/s00603-019-01947-w).
- [36] H. Yang, J. Ni, C. Chen, and Y. Chen, Weathering assessment approach for building sandstone using hyperspectral imaging technique, *Heritage Sci.*, vol. 11, no. 1, pp. 70, 2023b. DOI: [10.1186/s40494-023-00914-7](https://doi.org/10.1186/s40494-023-00914-7).
- [37] H. Yang, C. Chen, J. Ni, and S. Karekal, A hyperspectral evaluation approach for quantifying salt-induced weathering of sandstone, *Sci. Total Environ.*, vol. 885, pp. 163886, 2023a. DOI: [10.1016/j.scitotenv.2023.163886](https://doi.org/10.1016/j.scitotenv.2023.163886).
- [38] H. Yang, K. Song, and J. Zhou, Automated recognition model of geomechanical information based on operational data of tunneling boring machines, *Rock Mech. Rock Eng.*, pp. 1–18, 2022. DOI: [10.1007/s00603-021-02723-5](https://doi.org/10.1007/s00603-021-02723-5).
- [39] C. Chen, H. Yang, K. Song, D. Liang, Y. Zhang, and J. Ni, Dissolution feature differences of carbonate rock within hydro-fluctuation belt located in the three gorges reservoir area, *Eng. Geol.*, vol. 327, pp. 107362, 2023. DOI: [10.1016/j.enggeo.2023.107362](https://doi.org/10.1016/j.enggeo.2023.107362).
- [40] K. Song, H. Yang, D. Liang, L. Chen, and M. Jaboyedoff, Step-like displacement prediction and failure mechanism analysis of slow-moving reservoir landslide, *J. Hydrol.*, vol. 628, pp. 130588, 2024. DOI: [10.1016/j.jhydrol.2023.130588](https://doi.org/10.1016/j.jhydrol.2023.130588).
- [41] D. Hu, H. Sun, P. Mehrabi, Y.A. Ali, and M. Al-Razgan, Application of artificial intelligence technique in optimization and prediction of the stability of the walls against wind loads in building design, *Mech. Adv. Mater. Struct.*, pp. 1–18, 2023. DOI: [10.1080/15376494.2023.2206208](https://doi.org/10.1080/15376494.2023.2206208).
- [42] J. Wu, Y. Yang, P. Mehrabi, and E.A. Nasr, Efficient machine-learning algorithm applied to predict the transient shock reaction of the elastic structure partially rested on the viscoelastic substrate, *Mech. Adv. Mater. Struct.*, pp. 1–25, 2023. DOI: [10.1080/15376494.2023.2183289](https://doi.org/10.1080/15376494.2023.2183289).
- [43] S. Han, D. Zheng, B. Mehdizadeh, E.A. Nasr, M.U. Khandaker, M. Salman, and P. Mehrabi, Sustainable design of self-consolidating green concrete with partial replacements for cement through neural-network and fuzzy technique, *Sustainability.*, vol. 15, no. 6, pp. 4752, 2023. DOI: [10.3390/su15064752](https://doi.org/10.3390/su15064752).
- [44] S. Han, Z. Zhu, M. Mortazavi, A.M. El-Sherbeeney, and P. Mehrabi, Analytical assessment of the structural behavior of a specific composite floor system at elevated temperatures using a newly developed hybrid intelligence method, *Buildings.*, vol. 13, no. 3, pp. 799, 2023. DOI: [10.3390/buildings13030799](https://doi.org/10.3390/buildings13030799).
- [45] J. Liu, M. Mohammadi, Y. Zhan, P. Zheng, M. Rashidi, and P. Mehrabi, Utilizing artificial intelligence to predict the superplasticizer demand of self-consolidating concrete incorporating pumice, slag, and fly ash powders, *Materials.*, vol. 14, no. 22, pp. 6792, 2021. DOI: [10.3390/ma14226792](https://doi.org/10.3390/ma14226792).
- [46] E. Taheri, P. Mehrabi, S. Rafiei, and B. Samali, Numerical evaluation of the upright columns with partial reinforcement along with the utilisation of neural networks with combining feature-selection method to predict the load and displacement, *Appl. Sci.*, vol. 11, no. 22, pp. 11056, 2021. DOI: [10.3390/app112211056](https://doi.org/10.3390/app112211056).
- [47] Y. Feng, M. Mohammadi, L. Wang, M. Rashidi, and P. Mehrabi, Application of artificial intelligence to evaluate the fresh properties of self-consolidating concrete, *Materials.*, vol. 14, no. 17, pp. 4885, 2021. DOI: [10.3390/ma14174885](https://doi.org/10.3390/ma14174885).
- [48] E. Taheri, A. Firouzianhaji, P. Mehrabi, B. Vosough Hosseini, and B. Samali, Experimental and numerical investigation of a method for strengthening cold-formed steel profiles in bending, *Appl. Sci.*, vol. 10, no. 11, pp. 3855, 2020. DOI: [10.3390/app10113855](https://doi.org/10.3390/app10113855).
- [49] A. Firouzianhaji, N. Usefi, B. Samali, and P. Mehrabi, Shake table testing of standard cold-formed steel storage rack, *Appl. Sci.*, vol. 11, no. 4, pp. 1821, 2021. DOI: [10.3390/app11041821](https://doi.org/10.3390/app11041821).
- [50] P. Mehrabi, S. Honarbari, S. Rafiei, S. Jahandari, and M. Alizadeh Bidgoli, Seismic response prediction of FRC rectangular columns using intelligent fuzzy-based hybrid metaheuristic techniques, *J. Ambient Intell. Humaniz. Comput.*, vol. 12, no. 11, pp. 10105–10123, 2021. DOI: [10.1007/s12652-020-02776-4](https://doi.org/10.1007/s12652-020-02776-4).
- [51] E. Taheri, A. Firouzianhaji, N. Usefi, P. Mehrabi, H. Ronagh, and B. Samali, Investigation of a method for strengthening perforated cold-formed steel profiles under compression loads, *Appl. Sci.*, vol. 9, no. 23, pp. 5085, 2019. DOI: [10.3390/app9235085](https://doi.org/10.3390/app9235085).
- [52] P. Mehrabi, M. Shariati, K. Kabirifar, M. Jarrah, H. Rasekh, N.T. Trung, A. Shariati, and S. Jahandari, Effect of pumice powder and nano-clay on the strength and permeability of fiber-reinforced pervious concrete incorporating recycled concrete aggregate, *Construct. Build Mater.*, vol. 287, pp. 122652, 2021. DOI: [10.1016/j.conbuildmat.2021.122652](https://doi.org/10.1016/j.conbuildmat.2021.122652).
- [53] A. Togholi, P. Mehrabi, M. Shariati, N.T. Trung, S. Jahandari, and H. Rasekh, Evaluating the use of recycled concrete aggregate and pozzolanic additives in fiber-reinforced pervious concrete with industrial and recycled fibers, *Construct. Build Mater.*, vol. 252, pp. 118997, 2020. DOI: [10.1016/j.conbuildmat.2020.118997](https://doi.org/10.1016/j.conbuildmat.2020.118997).

- [54] H. SafarPour, and M. Ghadiri, Critical rotational speed, critical velocity of fluid flow and free vibration analysis of a spinning SWCNT conveying viscous fluid, *Microfluid Nanofluid.*, vol. 21, pp. 1–23, 2017. DOI: [10.1007/s10404-017-1858-y](https://doi.org/10.1007/s10404-017-1858-y).
- [55] H. SafarPour, M. Hosseini, and M. Ghadiri, Influence of three-parameter viscoelastic medium on vibration behavior of a cylindrical nonhomogeneous microshell in thermal environment: an exact solution, *J. Therm. Stress.*, vol. 40, no. 11, pp. 1353–1367, 2017. DOI: [10.1080/01495739.2017.1350827](https://doi.org/10.1080/01495739.2017.1350827).
- [56] T. Sinmazçelik, E. Avcu, M.Ö. Bora, and O. Çoban, A review: fibre metal laminates, background, bonding types and applied test methods, *Mater Design.*, vol. 32, no. 7, pp. 3671–3685, 2011. DOI: [10.1016/j.matdes.2011.03.011](https://doi.org/10.1016/j.matdes.2011.03.011).
- [57] W. Yang, G. Yan, E. M. Awwad, and M. Al-Razgan. 2023c. AI-based solution on the efficient structural design of the graphene-platelets reinforced concrete ceilings, *Mech. Adv. Mater. Struct.*, pp. 1–24, DOI: [10.1080/15376494.2023.2217653](https://doi.org/10.1080/15376494.2023.2217653).
- [58] T. Liu, A. Wang, Q. Wang, and B. Qin, Wave based method for free vibration characteristics of functionally graded cylindrical shells with arbitrary boundary conditions, *Thin-Walled Struct.*, vol. 148, pp. 106580, 2020. DOI: [10.1016/j.tws.2019.106580](https://doi.org/10.1016/j.tws.2019.106580).
- [59] Y. Qu, X. Long, G. Yuan, and G. Meng, A unified formulation for vibration analysis of functionally graded shells of revolution with arbitrary boundary conditions, *Compos. Part B: Eng.*, vol. 50, pp. 381–402, 2013. DOI: [10.1016/j.compositesb.2013.02.028](https://doi.org/10.1016/j.compositesb.2013.02.028).
- [60] S. Sun, D. Cao, and Q. Han, Vibration studies of rotating cylindrical shells with arbitrary edges using characteristic orthogonal polynomials in the Rayleigh–Ritz method, *Int. J. Mech. Sci.*, vol. 68, pp. 180–189, 2013. DOI: [10.1016/j.ijmecsci.2013.01.013](https://doi.org/10.1016/j.ijmecsci.2013.01.013).
- [61] B. Qin, K. Choe, Q. Wu, T. Wang, and Q. Wang, A unified modeling method for free vibration of open and closed functionally graded cylindrical shell and solid structures, *Compos. Struct.*, vol. 223, pp. 110941, 2019. DOI: [10.1016/j.compstruct.2019.110941](https://doi.org/10.1016/j.compstruct.2019.110941).
- [62] T. Ye, G. Jin, S. Shi, and X. Ma, Three-dimensional free vibration analysis of thick cylindrical shells with general end conditions and resting on elastic foundations, *Int. J. Mech. Sci.*, vol. 84, pp. 120–137, 2014. DOI: [10.1016/j.ijmecsci.2014.04.017](https://doi.org/10.1016/j.ijmecsci.2014.04.017).
- [63] J.L. Sewall, and E.C. Naumann, An experimental and analytical vibration study of thin cylindrical shells with and without longitudinal stiffeners, *National Aeronautic and Space Administration*, vol. 4705, 1968.